3 The First Energy Transfer Process: Electron–Gas Interactions

3.1 The Plasma State

The interaction of an electric current with a gas leads to dissociation and ionization. A plasma consists of electrons, positively charged ions, and neutral gas atoms.

The definition of the plasma state is as follows [1].

'Plasmas are quasi-neutral multiparticle systems characterized by gaseous or fluid mixtures of free electrons and ions, as well as neutral particles (atoms, molecules, radicals) with a high mean kinetic energy of electrons or all plasma components ($\langle\varepsilon\rangle \approx 1\,\text{eV}$–$2\,\text{MeV}$ per particle), and a considerable interaction of the charge carriers with the properties of the system'.

Since the states of matter can be defined by the mean kinetic energy $\langle\varepsilon\rangle$ of the constituent particles there exists an energy threshold ε_n at the phase boundaries that marks the transition among states and can be treated as typical binding energies. A criterion of the existence of the nth state of matter is $\varepsilon_{n-1} \leq \langle\varepsilon\rangle \leq \varepsilon$. With increasing $\langle\varepsilon\rangle$, i.e. increasing temperature matter passes through the states $n = 1 \ldots 3$ (solid, liquid, gaseous), and finally, through ionization of gas atoms, free electrical charge carriers appear that characterize the systems as the 4th state of matter. We have arrived at a plasma.

While the plasma is electrically conductive, its overall charge is neutral. This quasi-neutrality is being maintained by strong electric fields. The neutrality restoring electric field can be estimated as follows [2].

If a cubic centimeter of a plasma contains n^* electrons than the total charge contained in a sphere of radius r is $Q = -(4/3)\pi r^3 n^* e$ ($-e$ is the Millikan elementary electron charge $= 1.6 \times 10^{-19}\,\text{C} = 4.8 \times 10^{-10}\,\text{ESU}$ (electrostatic charge units)). Assuming a centrosymmetrical charge distribution the total charge Q is concentrated at the centerpoint of the sphere. This charge generates an electric field of strength $E = Q/r^2$ at a distance r from the centerpoint. If $r = 1$ cm and $n^* = 10^{15}$ (thermal or 'hot' plasma, see below) than $E = -6 \times 10^8\,\text{V cm}^{-1}$. One of the characteristics of the state of quasi-neutrality of a plasma is the fact that the number of positive and negative charge carriers per unit volume equals each other. If n_1 is the number and $+Z$ e the individual charge of the Z-times positively charged ions than the condition of quasi-neutrality is $n^* = Z \times n_1$ or $|n^* - Z \times n_1| \ll n^*$. Since the ions generate

a field $+6 \times 10^8\,\mathrm{V\,cm^{-1}}$ the total electric field strength is zero in the state of quasi-neutrality. However, any slight deviation, for example by statistical density variations of a ratio $1{:}10^{-6}$ results in the occurence of an electric field strength of $10^{-6} \times 6 \times 10^8 = 600\,\mathrm{V\,cm^{-1}}$ that instantaneously restores the quasi-neutrality. Only the occurence of oscillations of very high frequency, for example a displacement current, leads to a spacial separation of the centres of the positive and the negative charge clouds because the ions with their relatively high masses cannot follow the high frequency oscillations anymore.

3.1.1 Characteristic Plasma Parameters

Since the plasma state occupies an extremely wide range of densities, temperatures and magnetic field strengths it is convenient to define several characteristic plasma parameters. Hereby microscopic and macroscopic parameters can be distinguished. The former refer to interactions between individual particles in a plasma, the latter to specific plasma properties in a continuum that can be described by the basic magnetohydrodynamic (MHD) equations. As we will see, based on the magnitude of these microscopic parameters the electron density–temperature–magnetic field space can be subdivided. The most important microscopic parameters are the Langmuir plasma frequency, ω_{Pl}, the Debye screening length, λ_{D}, the Landau length, l_{L}, the mean free path length, λ (collision length), and the collision frequency, ν_{c}.

3.1.1.1 Langmuir Plasma Frequency

From the one dimensional radial equation of movement of electrons

$$m^*(\mathrm{d}^2r/\mathrm{d}t^2) = -(4/3)\pi n^* \mathrm{e}^2 r \tag{3-1}$$

(m^* = mass of electron, n^* = number of electrons per cm^3) with the exponential relations $r(t) = r_0 \exp(i\omega t)$ it follows that the electrons in a plasma undergo harmonic oscillations with a frequency

$$\omega = [4\pi n^* \mathrm{e}^2/3m^*]^{1/2}. \tag{3-2}$$

More accurate 3D-calculations (see for example [2]) lead to the equation for the Langmuir frequency

$$\omega_{\mathrm{Pl}} = [4\pi n^* \mathrm{e}^2/m^*]^{1/2} \tag{3-3a}$$

or, in the SI system,

$$\omega_{\mathrm{Pl}} = [n^* \mathrm{e}^2/m^* \varepsilon_0]^{1/2}, \tag{3-3b}$$

where ε_0 = vacuum dielectric permittivity ($= 8.86 \times 10^{-12}\,\mathrm{A\,s\,V^{-1}\,m^{-1}}$).

3.1.1.2 Debye Screening Length

To obtain characteristic plasma properties the electric space charge effects must exceed those of the thermal movement of the carriers. Only then collective interaction phenomena can occur that distinguish a plasma from a normal gas or a cloud of charged individual particles. Simplified one-dimensional calculations yield

$$\text{div } \boldsymbol{E} = (\delta E_x/\delta x) = 4\pi\rho^*, \quad \rho^* = -n^*\mathrm{e} \tag{3-4a}$$

($E_x = E$, $E_y = E_z = 0$), and after integration

$$E = -4\pi n^* \mathrm{e} x. \tag{3-4b}$$

The displacement of an electron by a distance λ_D in the electric field generated by the n^* electrons per cm^3 leads to an increase in energy defined by

$$\int \mathrm{e}E \, \mathrm{d}x = 2\pi n^* \mathrm{e}^2 \lambda_D^2. \tag{3-5}$$

This energy increase equals the mean thermal energy per degree of freedom, kT, and from $2\pi n^* \mathrm{e}^2 \lambda_D^2 = kT/2$ it follows that

$$\lambda_D = [kT/4\pi \mathrm{e}^2 n^*]^{1/2}. \tag{3-6}$$

This quantity is called the Debye screening length, and can further be expressed as

$$\lambda_D = 6.905[T/n^*]^{1/2}. \tag{3-7}$$

Since λ_D can be defined as that distance from a point charge within which the potential of the charge decreases to the eth part as the result of space charge effects, it is also called the 'screening length' of the potential ($\phi(r) = r^{-1} \exp[-r/\lambda_D]$).

3.1.1.3 Landau Length

That distance from a point charge at which the vacuum electrostatic energy equals the kinetic energy kT is called 'critical distance' or Landau length: $l_L = \mathrm{e}^2/kT$. The necessary condition preventing a recombination of ions and electrons is $a > l_L$, i.e. the mean distance a between plasma particles must exceed the Landau length. Since on the other hand the distance of the electrostatic interaction of plasma particles is the Debye length λ_D, the relation $a > \lambda_D$ means that there is no cooperative interaction between particles, i.e. there is no plasma.

Assuming spherical and continuous charge distribution, the volume of interaction, the so-called *Debye sphere* is given by $(4/3)\pi\lambda_D^3$. The Debye sphere contains thus $(4/3)\pi\lambda_D^3 n^*$ electrons. In order to apply continuity conditions there is the requirement $(4/3)\pi\lambda_D^3 > 1$ or $\Lambda = (n^*\lambda_D^3)^{-1} \ll 1$ or $(n^*)^{-1/3} \ll \lambda_D$. If the 'plasma parameter' $\Lambda \ll 1$ a true plasma exists!

3.1.1.4 Collision Path Length

In electrically neutral gases only van der Waals forces play a role with short interaction distances. Thus collisions among two or more particles are generally negligible. In a plasma, however, electric forces occur whose interaction distances (Debye length) exceed those of the intermolecular van der Waals forces. All charged particles are interacting constantly with a cloud (Debye sphere) of surrounding particles. For a minimum particle density an average ('smeared out') electric field can be assumed, and calculations can be performed as if a particle is being scattered only by this averaged field. Thus all elastic collisions among particles can be treated as binary collisions.

In general, plasma particles can collide inelastically and elastically. During *inelastic collisions* the total kinetic energy of a particle changes by transferring a portion of it to internal energy. Such inelastic collisions are responsible for excitation, ionization, recombination and charge transfer in plasmas. The hallmark of an *elastic collision* of particles is the conservation of its total kinetic energy. Such collisions occur predominantly in neutral gases at low temperatures.

The number of collisions per cm^3 and per second is determined by $\sigma(v)nF$, where $\sigma(v)$ is the collision cross-section, n is the number of scattering particles per cm^3 and F is the number of particles per cm^3 and per second that are being scattered. The mean free path length λ is the average path length traversed by a particle between two collisions. From the laws of kinetic gas theory it follows that $\lambda = [n\sigma(v)]^{-1} = kT/p\sigma(v)$, where p is the plasma pressure. For $p = 1$ atm and $T = 300$ K, λ is about 0.4 μm.

For elastic collisions the cross-section depends on the relative velocity ω of the particles and the scattering angle χ. However, assuming Coulomb forces limited by a finite value of λ_D, a mean free path length λ can be calculated independent of the scattering angle:

$$\lambda = [0.6 \times 10^6 T^2]/[n \ln(\lambda_D/l_L)] \approx (1.3 \times 10^4 T^2/n). \tag{3-8}$$

The term $\ln(\lambda_D/l_L)$ is called the *Coulomb logarithm* Λ_c. The particle velocity can be expressed through the temperature for a Maxwell–Boltzmann distribution as $m^* u^2 = kT$. For a thermal plasma ($T_e = T_h$; see Fig. 3-1) it follows that $\lambda_{Ion}/\lambda_{El} = m_{Ion}/m^*$, and for a collision angle of 90° $\lambda_{90} = (4\pi l_L^2 n)^{-1}$. With $l_L = e^2/kT$ and $\lambda_D = (kT/4\pi e^2 n^*)^{1/2}$ we obtain

$$\lambda_D^2 = \lambda_{90} l_L. \tag{3-9}$$

Combination with the inequalities expressed above leads to the *definition of a plasma*:

$$l_L \ll \lambda_D, \quad (n^*)^{-1/3} \ll \lambda_D, \lambda_D \ll \lambda_{90}. \tag{3-10}$$

Furthermore the condition $\Lambda \approx l_L/\lambda_D = \lambda_D/\lambda_{90} \ll 1$ must be fulfilled.

In addition to these conditions, another one has to be fulfilled. To treat a plasma as a continuous medium all statistical fluctuations must be alleviated to obtain a

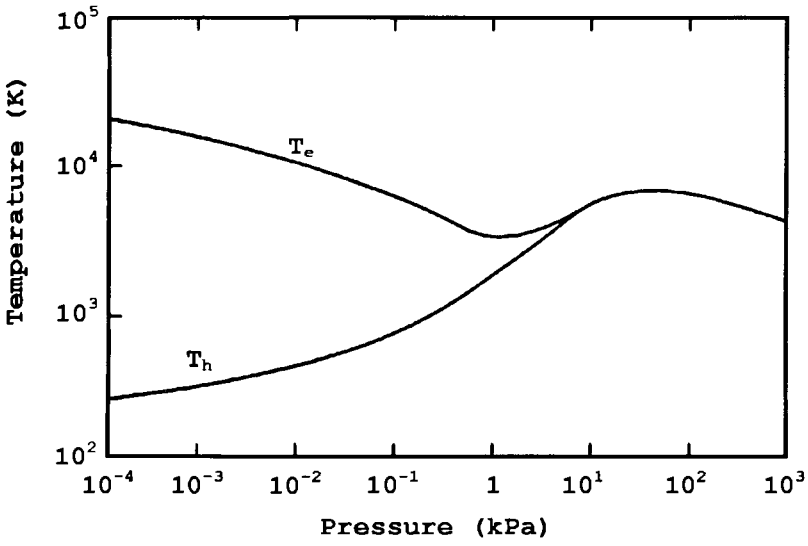

Figure 3-1. Electron (T_e) and heavy particle (T_h) temperatures as a function of pressure [3].

Maxwellian distribution of particle velocities. This requires frequent collisions of particles. The characteristic dimension of the plasma cloud, l, must be large compared to the collision length λ in order to guarantee many collisions: $\lambda \ll l$.

3.1.1.5 Collision Frequency

The velocity distribution of particles within a plasma is given, under equilibrium conditions, by a Maxwell distribution. The mean velocity $\bar{u}$ is defined by the thermodynamic temperature

$$\bar{u} = (8\,\mathrm{k}T/\pi m)^{1/2}; \quad \bar{u}^2 = 3\,\mathrm{k}T/m. \tag{3-11}$$

Without applied strong magnetic fields a particle in a plasma moves between two collisions in a force-free fashion, i.e. with constant speed $\bar{u}$. The relaxation time τ between two collisions is $\tau = \lambda/\bar{u} \sim T\sqrt{T}/n$, and for the collision frequency ν_c we obtain $\nu_c = \tau^{-1} = \bar{u}/\lambda$, or in terms of the collision cross-section, $\nu_c = n\bar{u}\sigma(v)$. Introducing the plasma parameter $\Lambda \approx l_L/\lambda_D$, and using the expressions for the Langmuir frequency ω_{Pl}, the Debye length λ_D and $\mathrm{k}T \approx m\bar{u}^2$ it follows

$$\Lambda \approx \lambda_D/\lambda \approx \nu_c/\omega_{Pl}. \tag{3-12}$$

3.1.2 Classification of Plasmas

Depending on the electron density, it is possible to distinguish low-pressure 'cold' (nonthermal) plasmas found in outer space with electron densities typically around

10^{-2} electrons per cm^3, and high pressure 'thermal' plasmas with electron densities exceeding 10^{18} electrons per cm^3 (Fig. 3-2). Thermal plasmas have pressures high enough to facilitate energy exchanges among light, fast moving and therefore energetic electrons and heavy, slowly moving charged ions. This energy exchange leads to efficient transfer of energy, increasing the plasma temperature, and thus reaching equilibrium. In such plasmas the electron temperature T_e equals the heavy particle temperature T_h; the plasma is in general or local thermodynamic equilibrium, and can be described according to the laws of thermodynamics (Fig. 3-1). The behavior of such a plasma is predictable. The energy extracted by the electrons from the electric field is transferred to enthalpy and, in turn, to an increase in temperature.

3.1.2.1 Low Density Plasmas

The variation of particle number per cm^3 (particle density) and temperature can be expressed by the plasma parameter Λ (see above). If $\Lambda \ll 1$, the plasma condition $\lambda \ll l$ is not guaranteed. In this case the number of collisions is low. If $\lambda > l$ than low density conditions prevail. Such a plasma is called a collision-free or Vlasov plasma (Fig. 3-3). Its relaxation time is $\tau = l(m/2kT)^{1/2}$.

3.1.2.2 Medium Density Plasmas

With increasing particle density the mean free collision paths decrease. If $\lambda \approx l$, medium density plasmas can be stabilized depending on the strength of the magnetic field. In a homogeneous static magnetic field an electrical charge describes a circular path around the field lines. The radius of this path is called the radius of gyration (Larmor radius) and given by

$$r_L = (muc/eB) \approx (8\,kTm)^{1/2}/eB(\pi)^{1/2}, \tag{3-13}$$

where u = linear circular velocity perpendicular to **B**, c = velocity of light, m = particle mass, B = magnetic field. For $M = m^*$, and with $m^*u^2 = kT$, the Larmor radius of an electron is

$$r_L^* = 3.7 \times 10^{-2}(\sqrt{T}/B). \tag{3-14}$$

The Larmor radius of a proton is $r_{L,Prot} = 1.6\sqrt{T}/B$. Assuming local thermal equilibrium, i.e. $T_e = T_h$, it follows that $r_{L,Ion} = r_L^*(m_{Ion}/m^*)^{1/2}$. Thus it is always true that $r_{L,Ion} > r_L^*$. The rotation frequency (cyclotron or Larmor frequency) is $\omega_L = eB/mc$.

For a low density plasma with $\lambda_D \ll \lambda$ or $l_L \ll \lambda_D$ (plasma condition) and $l \ll \lambda$ (low density condition), and in the presence of a weak magnetic field, r_L is relatively large but because of $l \ll \lambda$ always small compared to λ. With increasing field strength B, r_L decreases and fulfills even more the condition $r_L \ll \lambda$. This means that a charged particle undergoes many Larmor rotations before a collision occurs that knocks it off its cyclotron path. Collisions therefore influence a low density plasma at a high magnetic field only marginally.

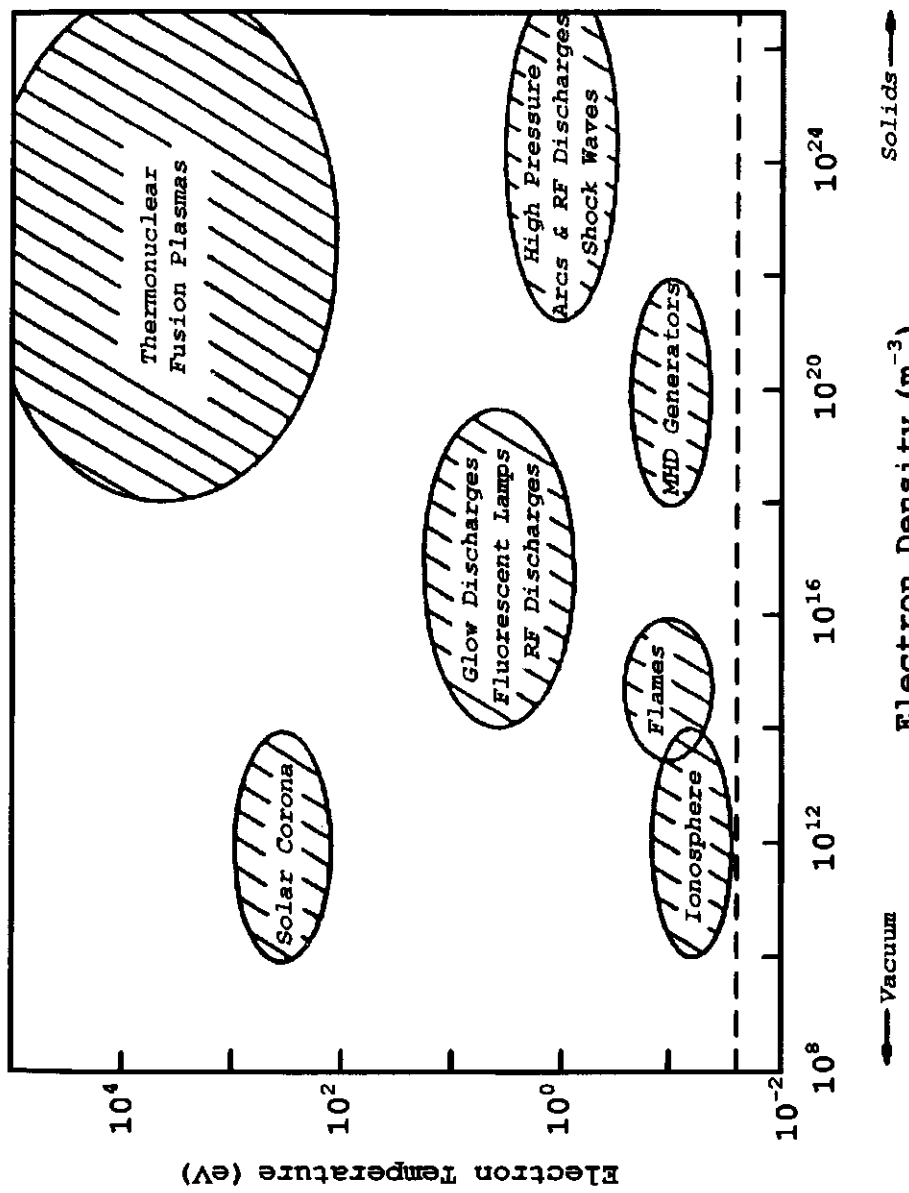

Figure 3-2. Classification of plasmas as a function of electron temperature and electron density [3].

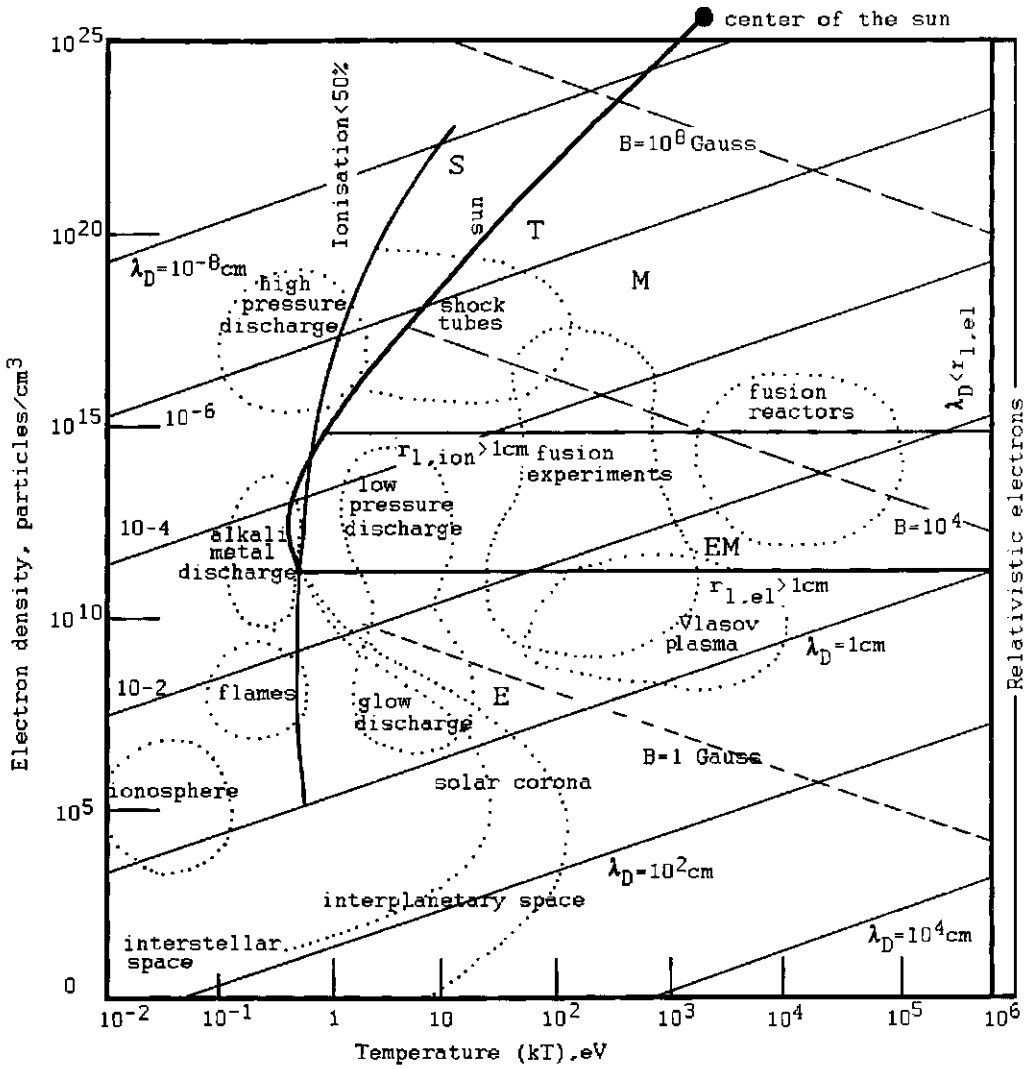

Figure 3-3. Possible states of a plasma [2].

A medium density plasma is characterized by $\lambda_D \ll \lambda$, $l_L \ll \lambda_D$ (plasma condition) and $l \gg \lambda$ (medium density condition). Depending on the strength of the magnetic field four plasma types can be distinguished: *electric* plasmas (E) ($l < r_L^*$ and $l < r_{L,Ion}$), *electromagnetic* plasmas (EM) ($l > r_L^*$, $l < r_{L,Ion}$), *magnetic* plasmas (M) ($l > r_L^*$, $l > r_{L,Ion}$; $\lambda_{El} > r_L^*$, $\lambda_{Ion} > r_{L,Ion}$) and *tensorial* plasmas (T) ($\lambda_{El} \gg r_L^*$, $\lambda_{Ion} < r_{L,Ion}$). The ranges of existence of these plasma types are shown in Figure 3-3. For a more detailed description, see textbooks on plasma physics and magneto-hydrodynamics.

3.1.2.3 High Density Plasmas

If the density increases so that $\lambda_{El} \ll r_L^*$, $\lambda_{Ion} \ll r_{L,Ion}$ then collisions outdo all anisotropic effects. In contrast to a tensorial plasma mentioned above any direction-dependent properties will cease to exist, and a '*scalar*' (isotropic) plasma (S) (see Fig. 3-3) evolves that can be described by the laws of fluid dynamics. Depending on the temperature, i.e. the degree of ionization 'two-fluid' (electrons and ions) or 'three-fluid' (electrons, ions and neutral particles) plasmas exist. In plasmas of extremely high densities ($n^* > 10^{19}\,cm^{-3}$) squeezing of charges can lead either to *recombination*, i.e. formation of a neutral gas or to *condensation*, i.e. formation of a solid state plasma.

Table 3-1 shows the classification of plasmas according to the characteristic plasma parameters, the electron density, temperature, magnetic field and characteristic distance, l [2]. Figure 3-3 shows the state of a plasma in an electron density–temperature net. Also shown are straight lines of equal Debye lengths ($10^{-8} < \lambda_D < 10^4$ cm) and magnetic field strengths ($1 < B < 10^8$ Gauss). Relativistic effects (particle velocity $u > 0.9c$) can be neglected for $T < 10^8$ K; quantum effects are negligible for $T_e > 6 \times 10^{-11} n^{2/3}$, $T_h > 3.2 \times 10^{-14} n^{2/3}$. The ranges of existence of the plasma types E, EM, M, T and S are also shown.

The plasma parameters, i.e. densities and temperatures of the charged species can be derived, in principle, by using an electric or Langmuir probe [4] Such a probe consists of a single electrode whose voltage–current characteristics are measured when it is surrounded by plasma [5]. In practice, the measurement of the densities and temperatures of the charged species reduce to the bulk ionization density n_0 and the electron temperature T_e.

3.1.3 Equilibrium and Nonequilibrium Plasmas

Extremely low pressure plasmas occuring in the interstellar space (10^{-2} e per cm^3) and low pressure 'cold' plasmas generated under moderate vacuum conditions are *nonequilibrium* or *two-temperature* plasmas. They are characterized by the fact that the electron temperature T_e is much greater than the heavy particle temperature T_h. The electron temperature is measured in eV where 1 eV is the energy gained by an electron when passing through a potential difference of 1 V. The kinetic temperature can be calculated from the mean particle energy $\langle\varepsilon\rangle$: $kT_K = (2/3)\langle\varepsilon\rangle$ (1 eV corresponds to 7 733 K or 1.6×10^{-19} J). Frequently the kinetic temperature of a plasma is given in terms of the most probable particle velocity, c_{Pr} : $kT_K = (1/2)\, mc_{Pr}^2$ (1 eV corresponds to 11 600 K). The electron density of a low pressure plasma is typically $< 10^{14}$ per cm^3, the electron temperature between 10^{-1} and 10 eV.

At a soft vacuum or atmospheric pressure thermal or 'hot' plasmas can be generated the electron temperature of which is of the order of the heavy particle temperature. Therefore such plasmas are called *equilibrium plasmas*.

The application of both types of plasma in materials processing is as follows:

- Low pressure 'cold' plasmas:
  plasma etching in semiconductor processing,
  plasma-assisted vapor deposition (PAVD),
  plasma surface modification.

Table 3-1. Characteristic plasma parameters (see Fig. 3-3): from reference [2].

Plasma type	Electron density (n) [cm^{-3}]	Temperature (T) [K]	Debye length (λ_D) [cm]	Collision length (λ) [cm]	Langmuir plasma frequency (ω_{Pl}) [s^{-1}]	Collision frequency (ν_c) [s^{-1}]	Magnetic field (B) [Gauss]	Larmor radius (r_L) [cm]	Characteristic distance (l) [cm]	Type of plasma
Interstellar gas	$1 \ldots 10^2$	10^4	10^3	1.3×10^{12}	5×10^4	10^{-4}	10^{-6}	3.7×10^6	10^{22}	Low to medium density M, EM
Interplanetary gas	10^2	10^5	10^2	1.3×10^{12}	5×10^5	10^{-3}	10^{-4}	10^5	10^{13}	Low to medium density M, EM
Ionosphere F-layer	10^6	10^3	10^{-1}	1.3×10^4	5×10^7	10^3	0.2	5	10^6	Medium density E, M, EM
Solarcorona	$10^6 \ldots 10^8$	10^6	10	1.3×10^{10}	5×10^8	10^2	10^{-4}	3.7×10^5	10^{11}	Low density
Hot plasma, diluted	10^{12}	10^6	10^{-2}	1.3×10^4	5×10^{10}	10^5	10^3	3.7×10^{-2}	10^3	Low density
Gas discharge	10^{14}	10^4	10^{-4}	1.3×10^{-1}	5×10^{11}	10^8	10^3	3.7×10^{-3}	10^2	Medium density EM, T
Dense hot plasma	10^{16}	10^6	10^{-4}	1.3	5×10^{12}	10^9	10^4	3.7×10^{-3}	10^3	Medium density T
Fusion plasma	$10^{15} \ldots 10^{17}$	10^8	10^{-3}	1.3×10^4	5×10^{12}	10^6	3×10^5	1.2×10^{-3}	10^3	Low to medium density EM
Air, standard conditions	10^{19} (atoms)	300	–	6×10^{-6} [a]	–	6×10^9	–	–	10^3	Ultrahigh density
Liquid mercury	10^{23}	10^2	10^{-10}	1.3×10^{-15}	10^{16}	10^{15}	10^3	3.7×10^{-4}	10	High density S
Interior of stars	$10^{22} \ldots 10^{25}$	10^8	10^{-6}	1.3×10^{-2}	10^{16}	10^{12}	$10^4 \ldots 10^8$	3.7×10^{-4}	10^{11}	Medium to high density M, T

[a] In air the mean free path length is calculated from $16n\sigma\lambda = 3$ or $3\eta = \lambda\rho u$ where η = viscosity, n = electron density, σ = collision cross-section, λ = collision length, ρ = density, u = velocity.

- High pressure 'hot' plasmas:
  plasma spraying,
  plasma spheroidizing,
  plasma chemical synthesis for ultrapure ceramic powder production.

3.1.4 Maxwellian Distribution of Plasma Energies

The electrons and the heavy particles will both establish a characteristic Maxwellian energy distribution. Under steady state (stationary) conditions the 'temperature' of a plasma is defined by the mean kinetic particle energy given by the equation $(3/2)kT = (m/2)u^2$ (see Eq. 3-11). Since the colliding particles change their velocities there is no universal particle velocity but only an averaged value $(\bar{u}^2)^{1/2}$.

A Maxwell distribution shows the fraction f of the plasma particles with a kinetic energy or velocity within the interval ε and $\varepsilon + d\varepsilon$ (or v and $v + dv$). Despite the continuous collisions this fraction is time invariant even though different particles will contribute to the overall distribution at any one time. Figure 3-4 shows the dependence of $f(\varepsilon)$ on ε for various mean energies $\bar{\varepsilon}$. The relationship between the velocity v and the kinetic energy ε is $\varepsilon = (m/2)v^2$.

This velocity distribution (Maxwell distribution) is

$$f(v)\,dv = (2/\pi)^{1/2}(m/kT)^{3/2}v^2 \exp(-mv^2/2kT)\,dv, \tag{3-15}$$

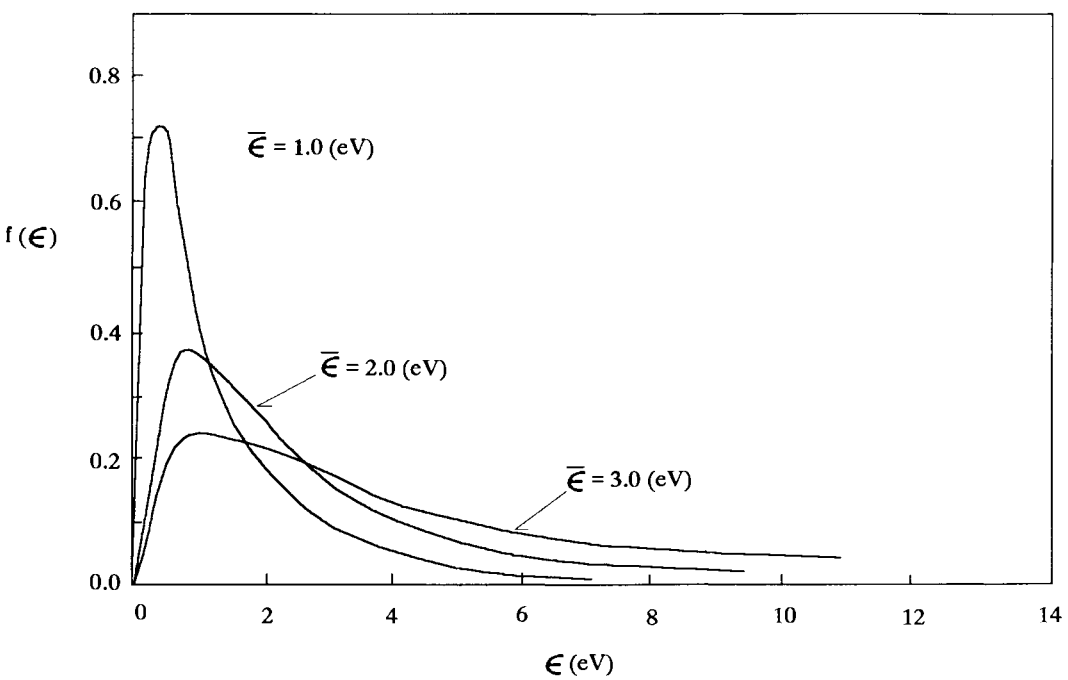

Figure 3-4. Maxwellian distribution of plasma particles.

or in terms of the kinetic energy ε,

$$f(\varepsilon)\mathrm{d}\varepsilon = 2/\sqrt{\pi}\,(\mathrm{k}T)^{-3/2}\sqrt{\varepsilon}\,\exp(-\varepsilon/\mathrm{k}T)\,\mathrm{d}\varepsilon. \tag{3-16}$$

The Maxwell distribution of plasma particles determines how many electrons have sufficient velocity and energy, respectively to extract energy from the electric field that is being transferred to enthalpy. It also determines the probability of collisions.

3.1.5 Equilibrium Compositions of Plasma Gases (Phase Diagrams)

Ionization of plasma gases takes place by a variety of processes chiefly among which are high energy radiation such as neutron beams, X-rays and ultraviolet radiation, collision processes in electric discharges, and also collision processes in intensively heated gases.

The ionization products assume a specific distribution in a particle density (number density)–temperature plot thus resulting in a phase diagram of ionization. Figure 3-5 shows such equilibrium distributions at 1 atm pressure of argon and nitrogen plasmas [6].

Figure 3-6 shows the energy content of typical plasma gases as a function of the temperature. This relationship is essentially linear but deviations from linearity occur due to ionization and dissociation. Monoatomic gases such as argon and helium need only to be ionized to enter the plasma state. Bimolecular hydrogen and nitrogen must first be dissociated. They thus need larger energy input to enter the plasma state. This enhanced energy will create increased enthalpy of the plasma. Small quantities of hydrogen or helium added as an auxiliary gas to argon lead to increased plasma enthalpy and thus increased heat transfer rates from the plasma to the powder particles. As a result, the plasma is hotter, and particles melt easier and more complete. Figure 3-7 shows the specific heat of various plasma gases at constant pressure as a function of the temperature. It can be seen that the high specific heat of helium and, in particular hydrogen increases the heat transfer rate.

3.2 Plasma Generation

The different methods of plasma generation are applications of gas ionization. In principle, energy will be transferred to atoms or molecules in an elementary process that is sufficient to initiate ionization. There exist two basic mechanisms.

- Increase of the energy content of all internal degrees of freedom of the gas by application of heat. This application can be accomplished directly through the container walls, or indirectly through chemical processes, compression or an electrical current. Plasma is generated by collision ionization of the particles and photoionization of the electromagnetic radiation in the hot gas. Such plasmas are generally close to their thermodynamic equilibrium state (isothermal plasmas).
- Transfer of energy for effective ionization without substantial temperature in-

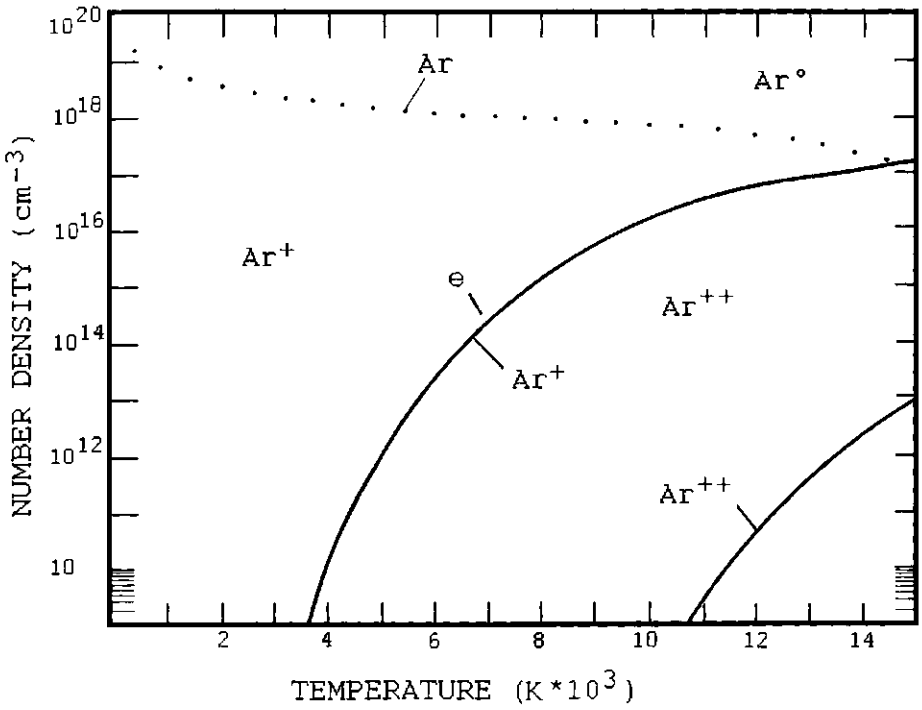

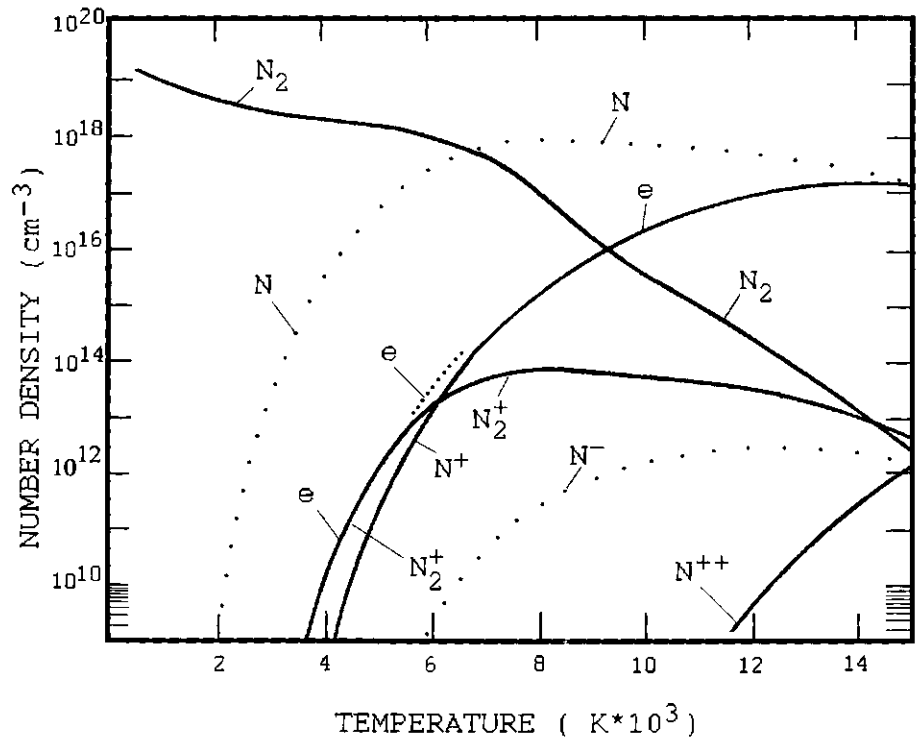

Figure 3-5. Equilibrium distribution (phase diagram) of argon (top) and nitrogen (bottom) plasmas [6].

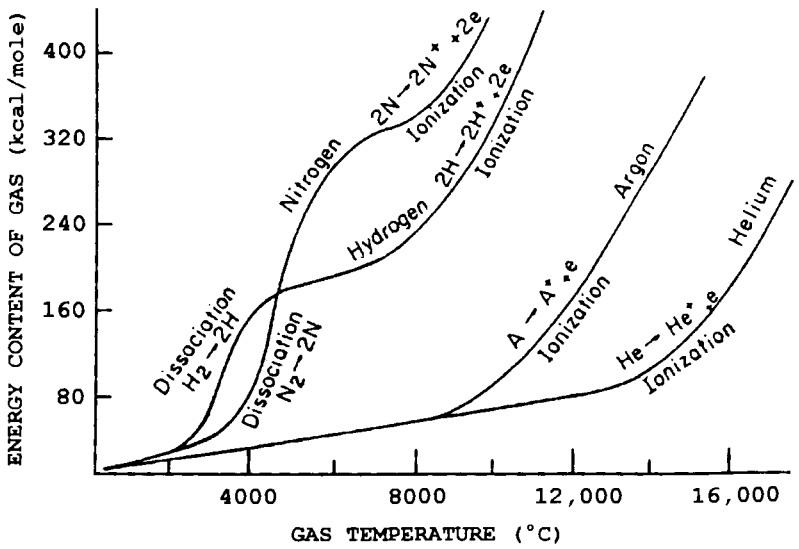

Figure 3-6. Energy content of typical plasma gases as a function of temperature [6].

crease of the gas through particle or electromagnetic radiation and electrical current, respectively. Such plasmas are nonequilibrium plasmas with a high electron temperature $T_e \gg T_{gas}$ (nonisothermal plasma).

Coupled mechanisms occur frequently during technical generation of plasmas.

3.2.1 Plasma Generation through Application of Heat

In a so-called *plasma furnace* (Fig. 3-8a) a gas is heated by temperature increase of the confining walls. A true thermal equilibium plasma forms whose degree of ionization, x, is determined by

$$x^2/(1-x^2) = 2(2\pi m^*/h^3)^{3/2}(g_1 E_0^{5/2}/g_0 p)(kT/E_0)^{5/2} \exp(-E_0/kT) \tag{3-17}$$

(Saha–Eggert equation), where m^* = mass of the electron, E_0 = ionization energy, p = gas pressure, and g_1 and g_0 = statistical weights of the ionization and the ground states, respectively.

Since the highest temperatures achievable are around 3 500 K, the degree of ionization is only about 1%. Thus this methods is confined to generation of low-energy plasmas for fundamental laboratory investigations.

An increase of the degree of ionization is possible by utilization of the contact ionization that occurs when the ionization energy of the atoms colliding with the hot

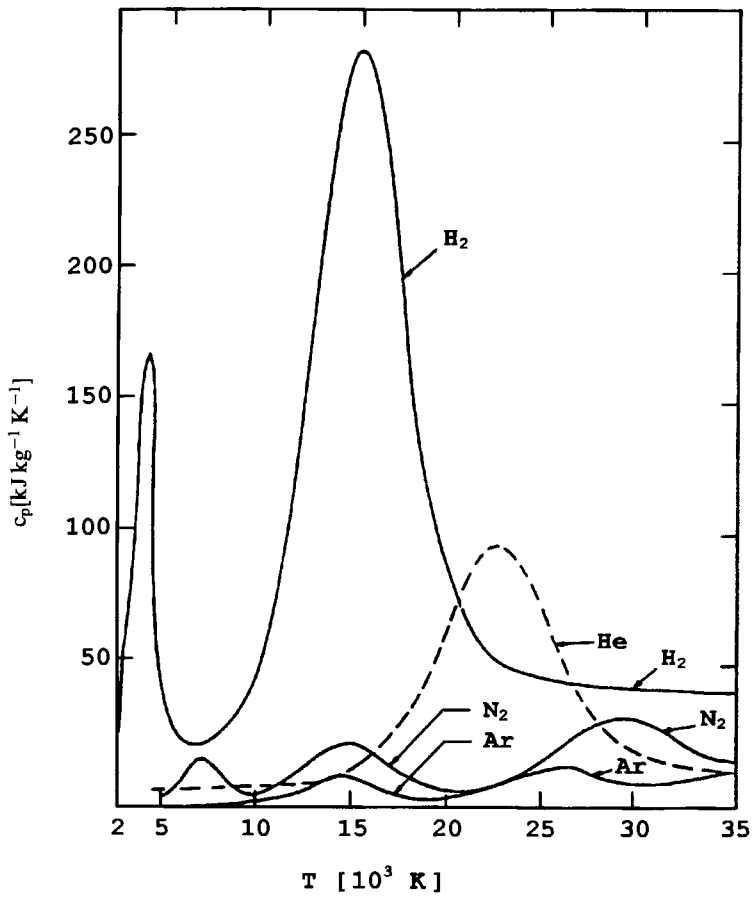

Figure 3-7. Specific heat of plasma gases at a constant pressure (1 atm) as a function of temperature [3, 6].

container walls is smaller than the work function, i.e. the thermionic electron emission energy of the wall material. For example, the ionization of cesium vapor atoms at heated tungsten plates leads to a noiseless ('quiet') plasma in which the reduction of the radial charge carrier losses of the plasma column is achieved through a longitudinal magnetic field (magnetic plasma confinement). The degree of ionization is up to 50%. Such a plasma generation device is called a 'Q-engine' (Q for quiet) (Fig. 3-8b).

Indirect heat transfer to a gas by exothermic chemical processes (flames, explosions) can yield stationary temperatures of up to 5 000 K. However, dramatically higher temperatures can be achieved during short times, for example, a strategic nuclear fusion device (H-bomb) can be triggered by the explosion of a nuclear fission device (Pu-bomb). Chemical reaction heat plasmas are being utilized in the MHD generator.

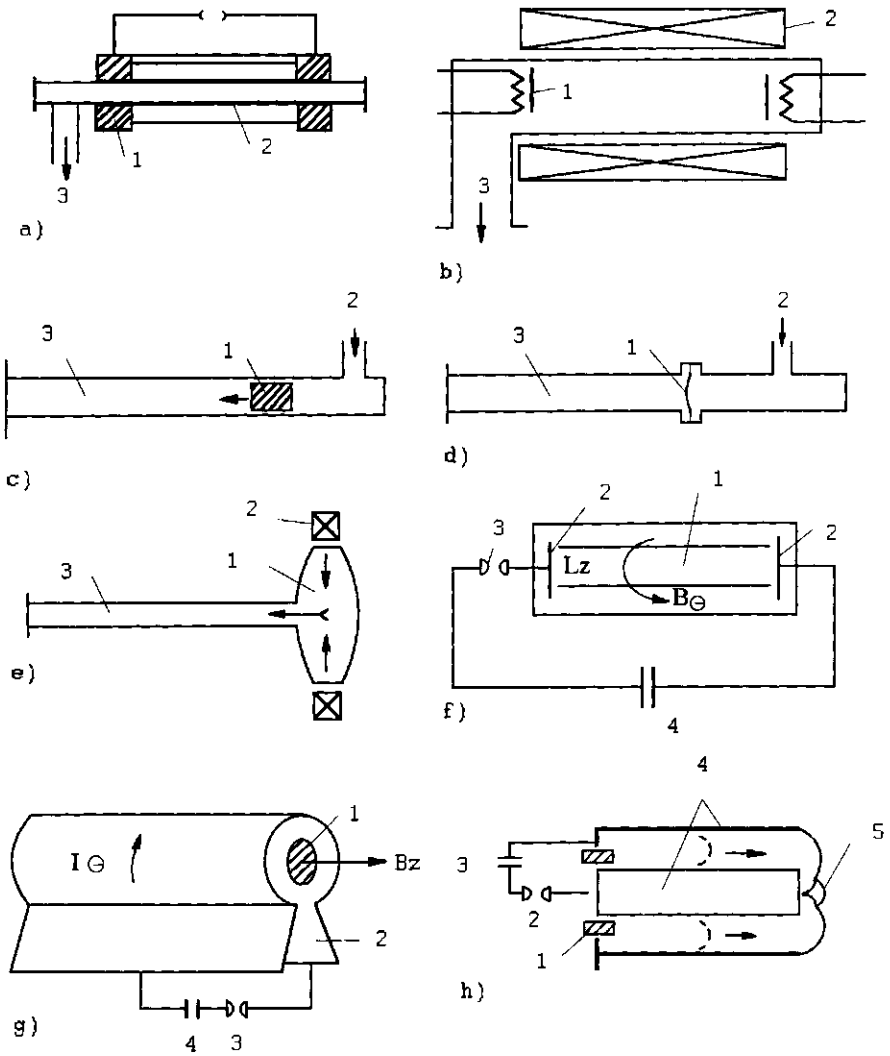

Figure 3-8. Principal ways of generating plasmas by heating (a,b) and compression of gases (c–h) [1]: (a) King's plasma furnace (1 electrodes, 2 graphite tube, 3 vacuum connection), (b) 'Q engine' (1 indirectly heated tungsten plates, 2 magnetic coil, 3 vacuum connection), (c) Ballistic compressor (1 sliding piston, 2 propellant gas inlet, 3 compression and observation section), (d) Mechanical shock tube (1 diaphragm, 2 high pressure gas inlet, 3 compression and observation section), (e) Inductive–hydrodynamic shock tube (1 discharge chamber, 2 shock coils for magnetic field, 3 compression and observation section). (f) z-pinch apparatus (1 plasma column, 2 electrodes, 3 arc gap, 4 capacitor battery), (g) Θ-pinch apparatus (1 plasma column, 2 one-turn coil, 3 arc gap, 4 capacitor battery), (h) Plasma focus (1 insulator, 2 arc gap, 3 capacitor battery, 4 electrodes, 5 focused plasma).

3.2.2 Plasma Generation through Compression

A ballistic compressor (Fig. 3-8c) consists of a tube a few meters long through which a piston of a few kilograms mass is accelerated by a burst of a propellant gas. The kinetic energy of the piston will be transformed to heat by adiabatic compression. Instead of the moving piston the compression can be achieved by a shock wave generated by bursting a membrane separating the high pressure from the low pressure region of the tube (Fig. 3-8d). For a short time temperatures of up to 5×10^4 K can occur.

In an electromagnetic shock tube (Fig. 3-8e) an oscillating magnetic field is used to generate ionization waves in a shallow chamber that propagate as a shock wave into the tube.

The so-called *pinch effect* refers to magnetic self-compression of a current-carrying plasma. In an impulse mode, temperatures up to 10^7 K can be generated in rapidly increasing magnetic fields. There are two principal configurations:

1. z-pinch (Fig. 3-8f).

Two planar electrodes conduct an axial current $\boldsymbol{j}_z$. The compression of the plasma occurs in the resulting magnetic field $\boldsymbol{B}_\theta$ by the inwardly directed Lorentz force, $F = (\boldsymbol{j} \times \boldsymbol{B}_\theta)$. In the regions of decreasing cross-section of the plasma column coupling of the Lorentz force and the pressure drop results in an axial force and consequently to the formation of a high velocity plasma jet. This mechanism is essential for the design of plasmatrons for plasma spraying machines.

2. Θ-pinch (Fig. 3-8g).

A current $\boldsymbol{j}_\Theta$ flowing through a coil generates an axial magnetic field $\boldsymbol{B}_z$ that compresses a plasma formed by pre-ionization.

3. Plasma focus (Fig. 3-8h).

This is a special variant of the z-pinch configuration in which the discharge of a capacitor battery in a coaxial electrode system leads to an electrodynamic acceleration of the plasma along the electrodes and a subsequent compression by radially directed forces.

3.2.3 Plasma Generation by Radiation

Gases can be ionized by interaction with energy provided by either particle radiation such as electrons or protons, or by electromagnetic waves. This kind of ionization is found in astrophysical plasmas.

In an electron beam plasma generator an energetic electron beam (keV range) will be focused on a diluted gas to provide, by collisional ionization, a plasma. Interaction of the beam with the plasma can generate turbulent Langmuir oscillations. In

the field of these oscillations the electrons of the plasma can acquire energy to form a nonisothermal plasma with a high electron temperature.

Gases can also by ionized in the optical range by application of powerful laser radiation. A focused laser beam produces at a threshold intensity of about $10^5\,\mathrm{MW\,cm^{-2}}$ a plasma in the focal plane in an explosive fashion by extension of the high frequency discharge beyond the microwave region (optical discharges).

3.2.4 Plasma Generation by Electric Currents (Gas Discharges)

The oldest and most important method of generating plasmas is by the formation of an electric current in a gas. The conversion of electrical energy in the various energy forms of a plasma is facilitated by the acceleration of charge carriers in an electric field with subsequent energy transfer by collision. According to the temporal behavior of the current there are several options:

- d.c. discharge mode,
- a.c. discharge mode, or
- impulse mode.

In the a.c. discharge mode the frequencies used range from technical a.c. current to the high frequency range to microwaves and optical frequencies to X-ray and γ-ray frequencies. In the d.c. discharge mode the current is being supplied to the gas discharge region directly through metallic electrodes whereas in the a.c. mode the electrodes can be separated from the gas region by a solid insulating material.

In general, gases are good insulators and to start a discharge free charge carriers must be generated or injected into the gas. In many cases the gas creates those carriers by self discharge. In other cases a plasma is being ignited by a high frequency impulse, i.e. a spark that ionizes the gas and creates enough charge carriers to sustain the electric discharge.

The static discharge characteristic of a gas column is shown in Fig. 3-9 in an I–V plot [1]. At small voltages a very small current flows based on external sources of ionization such as space ionization. In this range Ohm's law is valid in good approximation, i.e. I is linearly proportional to U. At larger currents deviations from Ohm's law occur if the loss of charge carriers due to their movement towards the electrodes cannot be neglected anymore compared to the generation of carriers by external sources of ionization. Beyond the saturation current $I = I_s = \text{const.}$ the characteristic enters a region of increasing current in which due to collisional ionization of electrons additional carriers will be generated in an avalanche fashion. Along a distance x the number of electrons formed by ionization increases to $\exp(\alpha x)$. In particular the multiplication along the electrode distance d is $M = \exp(\alpha d)$, where α is the first Townsend coefficient that is determined by the ionization frequency ν_i and the drift velocity v_e of the electrons ($\alpha = \nu_i / v_e$).

As long as the current is still dependent on the existence of an external ionization source to sustain the discharge despite the multiplication effect of charge carriers, the gas remains in the state of a *dependent discharge*. The ignition of an *independent dis-*

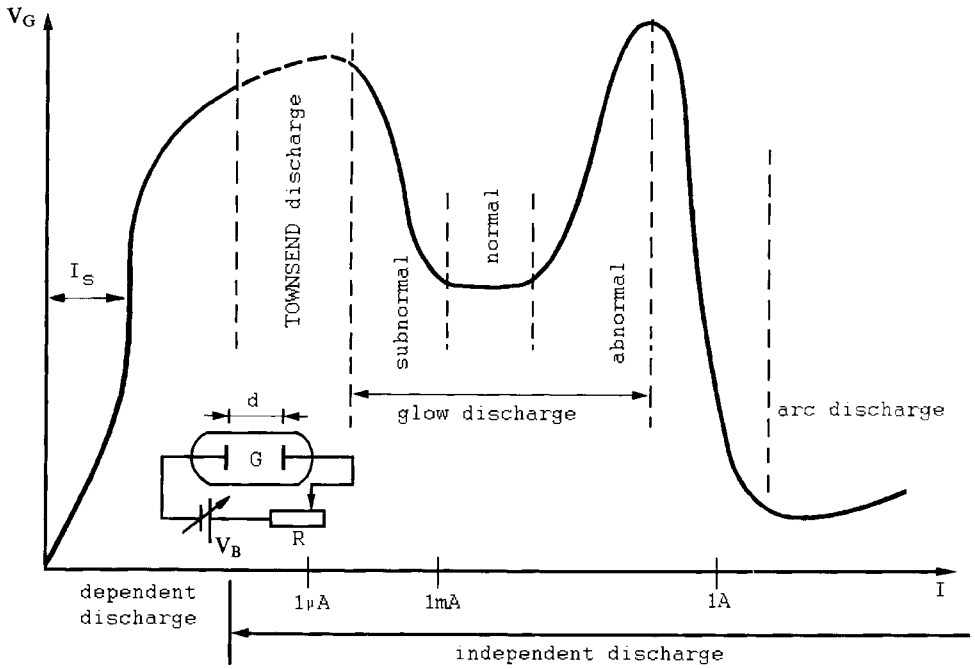

Figure 3-9. Complete static discharge characteristic of a gas [1].

charge is achieved by fulfilling the Townsend ignition condition, $\gamma[\exp(\alpha d) - 1] = 1$. The second Townsend coefficient γ considers all processes leading to the generation of secondary electrons, for example electron emission at the cathode by ion impact, photoelectrons, and the volume ionization by fast ions or photons.

In the range of small currents in the transitional range between the dependent and independent discharge there is the dark- or Townsend discharge (Fig. 3-9). It is characterized by lack of luminescence, small field displacement by space charges, and an almost horizontal I–U characteristic. With increasing current electrical space charge domains occur with a tendency to decrease the voltage. Dependent on the value of the current, two cathode mechanisms can be distinguished, the glow cathode with a small discharge current, and the arc cathode with a large discharge current.

3.2.4.1 Glow Discharges

Glow discharges occur in diluted gases ($p \approx 1$–10^4 Pa) at small currents ($I \approx 0.1$–100 mA). They lead to characteristic luminescent features between the electrodes that are divided into differently colored lighter and darker parts depending on the nature of the gas (cathode layer, Crooke's dark space, negative glow light, Faraday's dark space, positive column, anode glow light). In front of the glow cathode there is a strong space charge field called the *cathode fall*. In this region the electrons acquire the energy for ionization. The formation of the cathode fall at the transition from the

Townsend discharge to the glow discharge is associated with the decrease of the voltage (subnormal discharge, see Fig. 3-9). At higher currents the cathode fall obtains initially a minimum value independent on the current (normal cathode fall). The typical range of the normal cathode fall is between 100 and 300 V. When the cathode is being completely covered by the glow light, the cathode fall and the current density increase with increasing current again (abnormal cathode fall).

3.2.4.2 Arc Discharges

The glow discharge is of no consequence for the plasma spray process. At high current densities, however, the abnormal glow discharge is replaced by an *arc discharge*. The arc cathode acquires a high temperature that leads to thermal electron emission. Normally on the cathode a narrowly confined termination of the arc occurs as a bright and highly mobile spot with an extremely high current density up to $10^7\,A\,cm^{-2}$ and a low cathode fall of typically 10 to 50 V. Ions impinging on the cathode are responsible for sustaining the cathode temperature and thus electron emission. Heating of the cathode (thermal arc) is complemented by a field emission of electrons (field arc) generated by the space charge field of ions flowing towards the cathode. Typical values for the current densities required for thermal emission and field emission are, respectively 10^3–$10^4\,A\,cm^{-2}$ and 10^6–$10^8\,A\,cm^{-2}$ with characteristic temperatures of $>3\,500$ K (hot cathode with thermal emission) and $<3\,000$ K (cold cathode with field emission). In general the production of secondary electrons by collective processes at the arc cathode is much more effective than the individual processes occuring at the glow cathode.

Recent investigations have shown that nonsteady state electron emissions from the arc cathode may also play an important role. Such a mechanism is characterized by extremely fast heating of microscopic asperities at the cathode surface by Joule heating and ion impingement. The asperities evaporate explosively as a dense plasma and release a large quantity of charge carriers.

Accordingly, the electrical processes occuring in different parts of the arc discharge are complex and despite a considerable amount of research in the past [7] still the subject of controversy.

The potential distribution in the arc is shown in Fig. 3-10a with the existence of three main arc regions, namely a positive column extending over the major portion on the arc path with a constant field strength, a cathode fall region with a voltage drop $V_{c'}$ close to the cathode of a typical thickness $d_{c'}$ of about 1 mm and supporting a voltage of approximately 10 V, and an anode fall region of similar size with a similar voltage drop of $V_{a'}$. The layers d_c and d_a immediately adjacent to the surface of the cathode and anode, respectively are the thermal boundary layers or space charge zones with a typical thickness of 10^{-4} cm. They provide the greater part of the voltage drop. The remainder of the cathode and anode falls are also called the contraction zones. Figure 3-10b shows the extension of the space charge regions adjacent to the electrodes in the areas of the cathode and the anode falls. In general the gas pressure in arc discharges is much higher than in glow discharges (high pressure discharge, $p \geq 10^5$ Pa). The requirement for the existence of the positive column is a sufficiently large electrode distance. The high gas pressure in the positive column

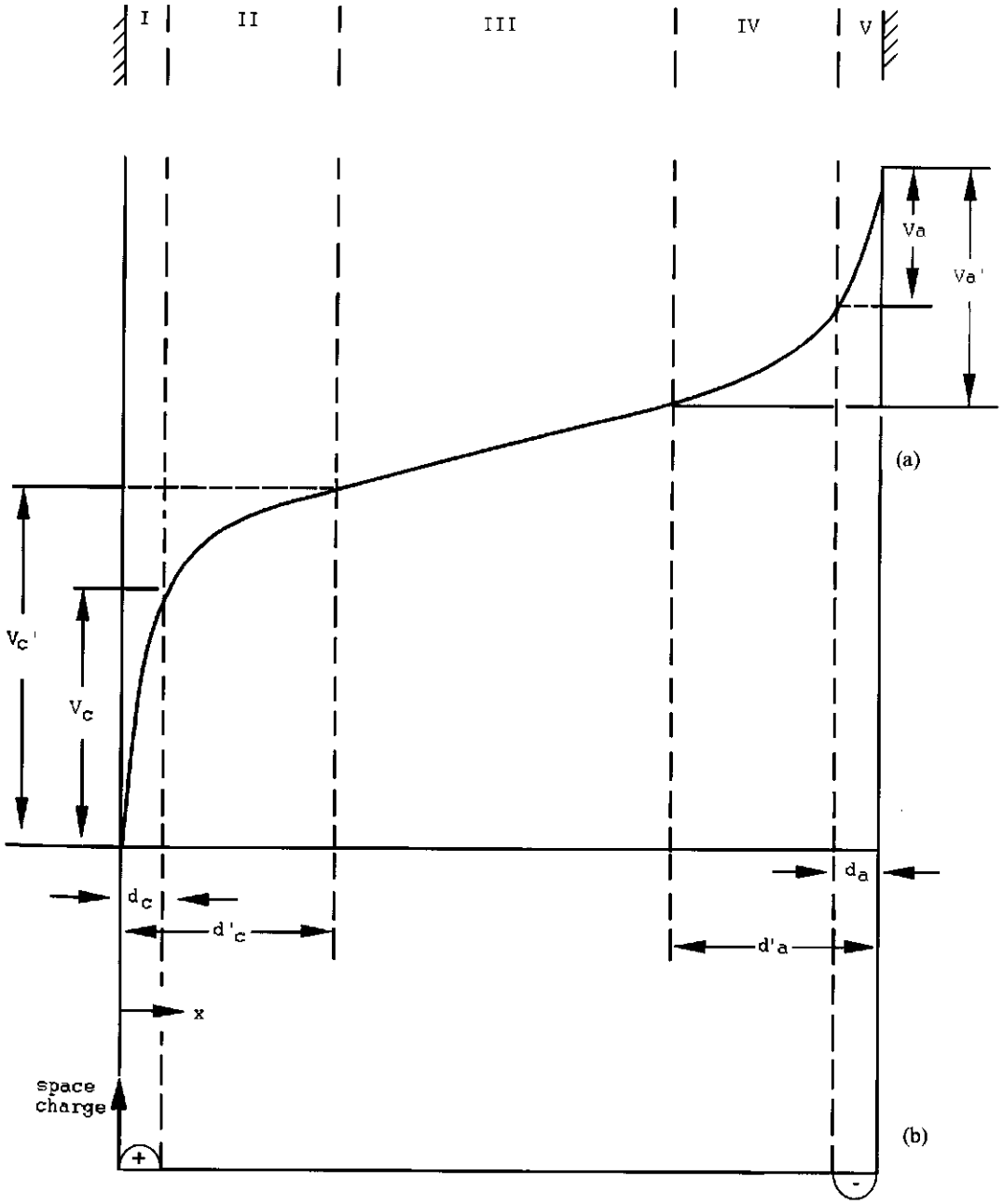

Figure 3-10. Potential distribution in an electric arc (a) and extension of the space charge region adjacent to the electrodes (b) (after [7]).

causes many collisions of ions that are responsible for an equalization of the electron and heavy particle temperatures (thermal plasma, see above).

3.2.4.3 Modeling of the Arc Column

In the case of a thermal equilibrium, the calculation of the characteristic plasma parameters can be performed assuming thermodynamic equilibrium conditions. In particular, rather simple modeling of the arc column was performed by Elenbaas [8] and Heller [9] already in the 1930s by equating the temperature gradient in the arc column with the generating electrical field:

$$\operatorname{div}(-\lambda \operatorname{grad} T) - \sigma E^2 = 0, \tag{3-18}$$

where λ is the thermal conductivity, σ is the electrical conductivity, and E is the electrical field. It should be particularly emphasized that the actual situation in an arc column is too complex to be solved through the conservation equations of mass, momentum and energy. In the Elenbaas–Heller approach thermal diffusion and effects of radiation have been neglected. Assuming rotational symmetry and introducing cylindrical coordinates the equation reads

$$(1/r)\mathrm{d}/\mathrm{d}r\{r\lambda(\mathrm{d}T/\mathrm{d}r)\} + \sigma E_z^2 = 0. \tag{3-19}$$

With the definition of the heat flux potential, $S = \int \lambda \, \mathrm{d}T$ it follows that

$$(1/r)\mathrm{d}/\mathrm{d}r\{r(\mathrm{d}S/\mathrm{d}r)\} + \sigma E_z^2 = 0; S = S(\sigma). \tag{3-20}$$

With Ohm's law, $I = 2\pi E_z \int \sigma r \, \mathrm{d}r$ we arrive, following Maecker [10], at the closed-form solutions

$$I = Rf_1(S); E = (1/R)f_2(S), \quad \text{and also} \tag{3-21a}$$

$$IE = f_3(S) = f_4(T), \quad \text{from which follows} \tag{3-21b}$$

$$T_{\max} = f(IE), \tag{3-21c}$$

i.e. the maximum temperature in an arc depends only on the power input per unit length. Thus in contrast to a flame torch with a maximum achieveable temperature limited to that obtained from the internal enthalpy of the combustion gases, the maximum temperature of a plasmatron is basically unlimited. It only depends on the power input that itself is limited by the cross-section of the power leads. The modeling approach was taken from [3]. An experimental confirmation of the statement made above is shown in Fig. 3-11 that displays the almost linear dependence of the axial temperature of an hydrogen arc as a function of the power input in $\mathrm{kW\,m^{-1}}$.

More involved modeling using the simultaneous solution of the conservation equations as well as species diffusion and the Maxwell equations can only be performed assuming:

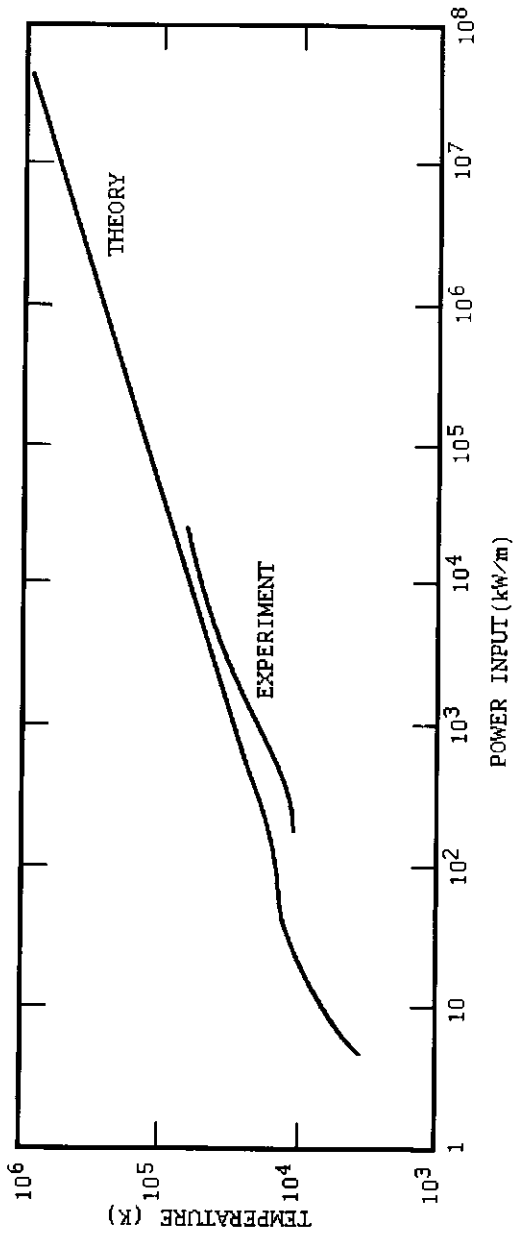

Figure 3-11. Maximum axial temperature in a hydrogen arc [10].

- 2D-rotational symmetry of the arc column,
- turbulent flow for d.c. plasmas,
- laminar flow, i.e. low Reynolds number *Re* for R.F. plasmas,
- optically thin arc,
- local thermal equilibrium, i.e. $T_e = T_h$,
- no viscous dissipation of the arc,
- negligible diffusion, and
- wall-stabilized arc conditions (see below).

Under these assumption it appears feasible to model the temperature and velocity profiles in a plasma arc column, and from this to predict particle trajectories, and heat and momentum transfer from the plasma to the particles (see Chapter 4). For details see, for example, Mostaghimi *et al.* [11] and Proulx *et al.* [12].

3.2.4.4 Structure of the Arc Column

Positive column

For a cylindrical symmetric column the field strength is constant and, according to Poisson's law the net space charge is zero (Fig. 3-10b). This indicates that the concentration of positive, n^+, and negative n^-, charges must be equal. The positive column thus satisfies the condition for a plasma (see above). The current flowing through the column will have two components, an electron current $\boldsymbol{J}^-$ and a positive-ion current $\boldsymbol{J}^+$. The total current density is

$$\boldsymbol{J} = \boldsymbol{J}^- + \boldsymbol{J}^+ = e(n^- \boldsymbol{v}^- + n^+ \boldsymbol{v}^+) = ne(\boldsymbol{v}^- + \boldsymbol{v}^+), \tag{3-22}$$

where $\boldsymbol{v}^-$ and $\boldsymbol{v}^+$ are the drift velocities produced by the electric field. The drift of the charged particles is impeded by collisions with neutral and other charge carriers. This represents a resistive phenomenon. Since $\boldsymbol{v}^- \gg \boldsymbol{v}^+$, the total current is carried predominantly by the electrons. Thus it follows that

$$\boldsymbol{J} \approx \boldsymbol{J}^- = n^- e \boldsymbol{v}^- = n^- e \mu \boldsymbol{E} = \sigma \boldsymbol{E}, \tag{3-23}$$

where μ is the electron mobility and σ the electrical conductivity.

The cathode fall region

To satisfy the continuity condition, the current flowing through the positive column must also make the transit from gas to metal at both electrodes. Hence in the cathode region conditions must exist that allow this transition. For refractory cathodes the mechanism is one of thermionic emission. There is a continuous and controllable transition from a glow discharge to an arc state depending upon the cathode temperature (Fig. 3-12, [13]). To lower the work function of the electrons, and to get an abundance of electron emissions to initiate and sustain the arc discharge, the cathode of a plasmatron is usually coated with thorium. Figure 3-13 shows the current char-

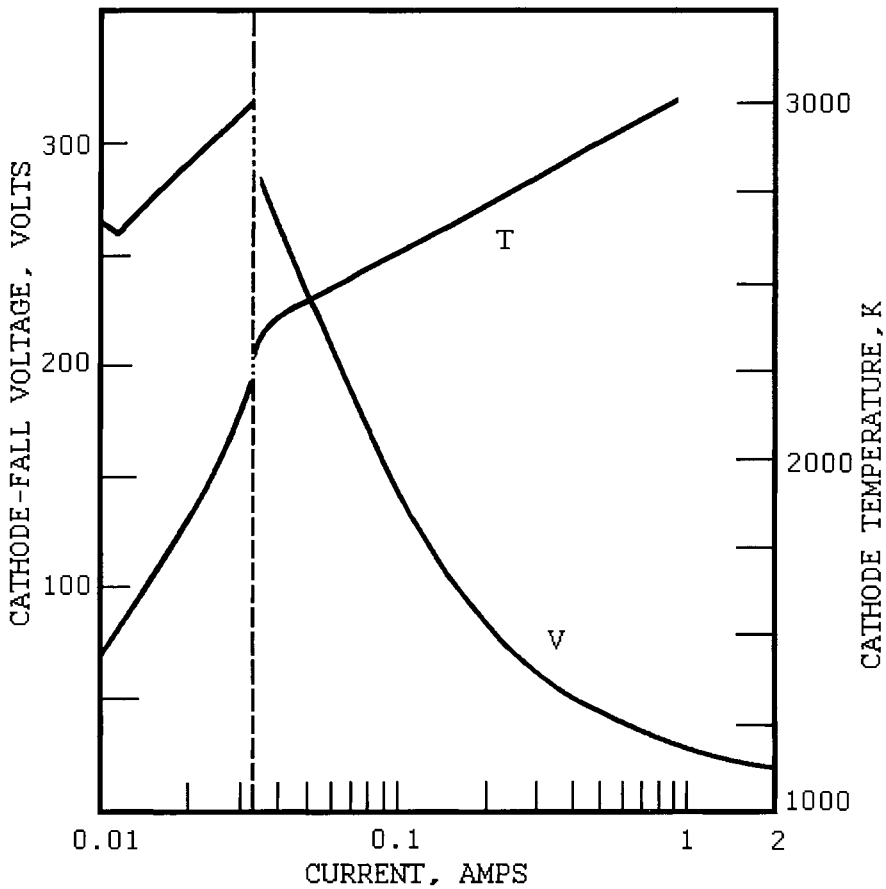

Figure 3-12. Variations of cathode-fall voltage and cathode temperature with the applied current during thermionic glow discharge-to-arc transition [13].

acteristic of thermionic electron emission in a vacuum diode. It can be described by the Richardson–Dushman equation

$$j_s = AT^2 \exp(-e\Phi_c/kT), \tag{3-24}$$

where A is the area of the electron emission and Φ_c is the electron work function. Because of the space charge region adjacent to the cathode the emission of electrons is impeded by the electric field on the cathode surface. Therefore the equation must be corrected. For high cathode temperature and moderate field strength the Schottky correction can be applied:

$$j_s = AT^2 \exp\{-[e\Phi_c - (e^3E/4\pi\varepsilon_0)^{1/2}]/kT\}. \tag{3-25}$$

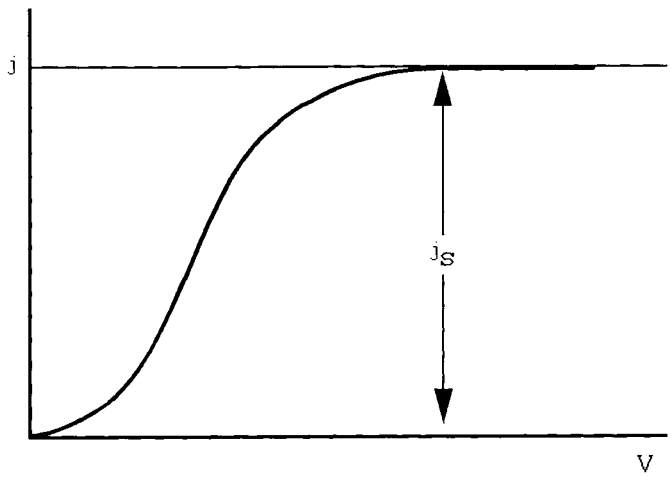

Figure 3-13. Current characteristic of thermionic electron emission in a vacuum diode.

The ability to emit electrons by thermionic emission differs among different metals. Figure 3-14 shows a plot of the thermionic work function Φ_c against the boiling temperature of the metal. Metals with particularly high work functions and thus thermionic emission are molybdenum, tungsten, tantalum and rhenium [14].

The net energy supplied to the cathode can be described by the balance between the current carried by the impinging ions and that caused by electron emission. The energy supplied to the cathode by impinging ions is

$$j_i(V_c + V_1 - \Phi_c + (5/2)kT_i/e, \tag{3-26a}$$

the energy removed by electron emission is

$$-j_e\Phi_c. \tag{3-26b}$$

This is, however, an idealization. The cathode also acquires energy from other sources such as neutralization energy transfer, condensation energy from the ions, heat conduction from the gas, radiation and possibly chemical reactions. The energy losses also encompass vaporization, loss of metal globules by thermal sputtering, radiation and heat conduction through both solid and surrounding gas.

The ratio j_i/j_e is between 0.15 and 0.5 depending on the cathode material and the electrical field strength.

As mentioned above, loss of material from the electrodes frequently occurs as do usually preferentially directed plasma arc jets. Such plasma jets may also be produced by constricting the diameter of a small section of the arc column. In this case the pressure gradient due to the pinch of the self-generated magnetic field increases with current density in the steady state. The constricting Lorentz force is directed inwardly and confines the plasma jet. This phenomenon will be discussed in detail later. Figure 3-15 shows the interaction of cathode and anode jets in an arc. The mode of attachment of the cathode arc jet at the surface of the cathode de-

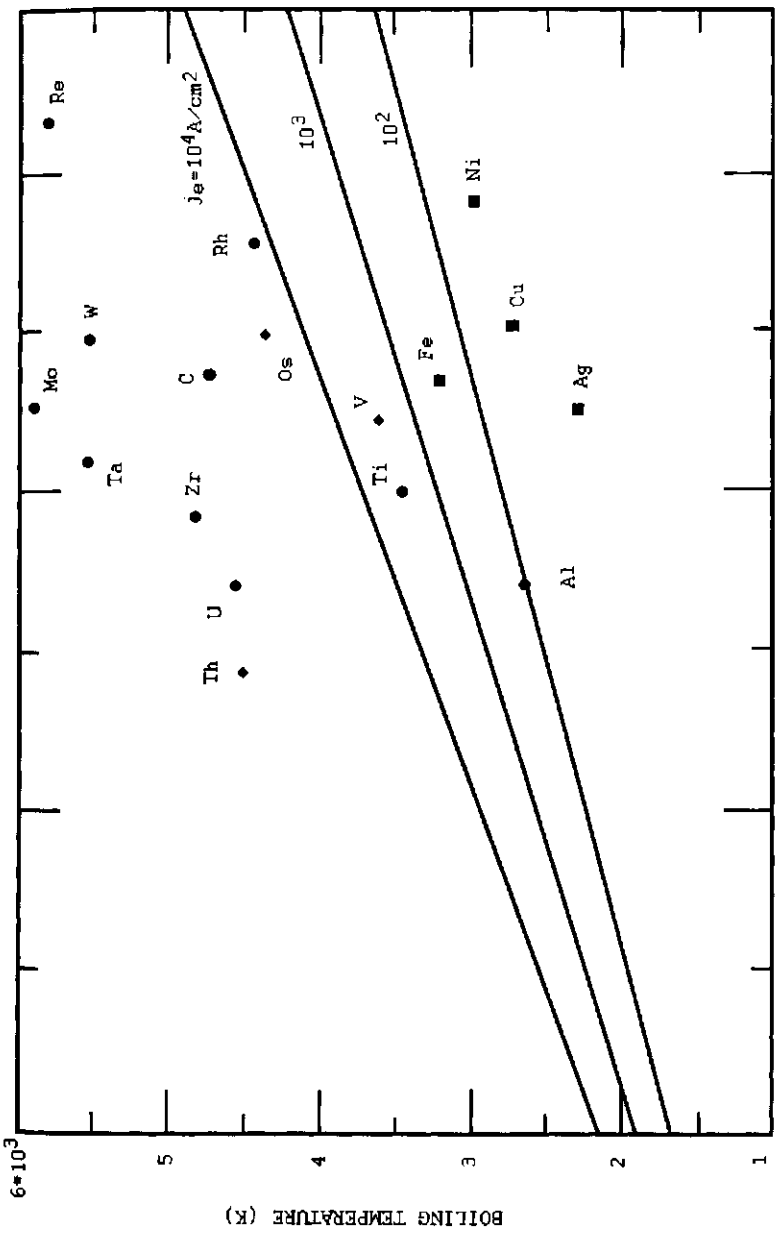

Figure 3-14. Thermionic work function, Φ_c, as a function of the boiling temperature of various metals [14].

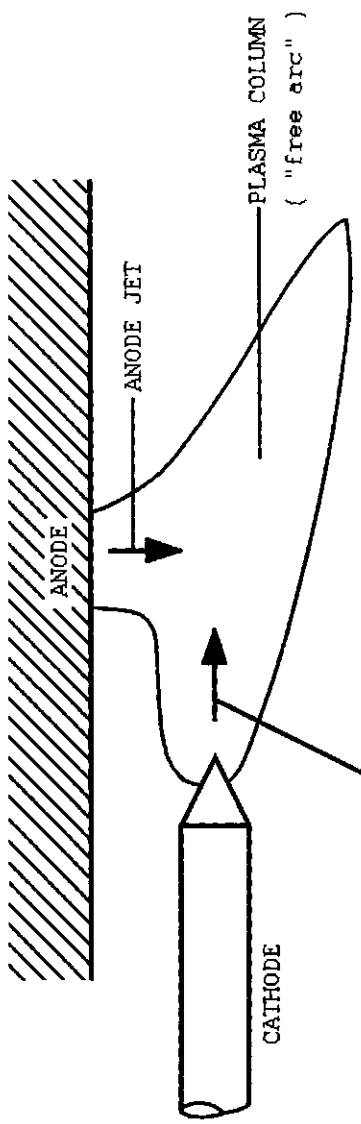

Figure 3-15. Interaction of cathode and anode jets in an arc [3].

pends on the current density. Diffuse attachment without localized spots occurs at 10^3–10^4 A cm^{-2} whereas distinct spots are visible at higher current densities (10^6–10^8 A cm^{-2}). In case of the attachment of the anode arc jet, lower current densities of 10^2–10^3 A cm^{-2} produce diffuse, higher ones (10^4–10^5 A cm^{-2}) constricted, i.e. spot-like attachment. Frequently the diffuse attachment of the anode arc jet is caused by the cathode jet impinging on the anode. This is known as the cathode jet-dominated (CJD) mode.

The anode region

Positive-ion emission from the anode can be neglected for most arc conditions. In this region current continuity is thus achieved by the total current being fed into the anode by electrons. This necessitates the production of extra electrons in the anode region. In many ways the anode region is similar to the cathode region even though the conditions are not so extreme. For example, the contraction zone is less sharp. The calculation of the energy balance at the anode is simpler than that at the cathode since a number of the coefficients involved are more definite. Most of the power is consumed in metal vaporization so that a high anode vapor pressure exists. This is then the source for the often observed anode vapor jets [8] (see Fig. 3-15) when the cathode arc jet impinging on the anode surface causes material to evaporate.

By introducing a diaphragm in front of the anode of a high-intensity argon arc the flow is interrupted thus resulting in the anode jet-dominated (AJD) mode. Temperature measurements based on line-emission coefficients and on absolute continuum-emission coefficients (see Sec. 3.4), and modeling by simultaneously solving the conservation equations under simplifying boundary conditions show reasonable agreement of the temperature distribution along the anode region (Fig. 3-16, [16]).

3.3 Design of Plasmatrons

Simplistically, one can visualize plasmatrons as resistance heaters in which familiar resistance elements such as nichrome, silicon carbide, tungsten etc. are replaced with a consumable, conductive and partially ionized gas. Thus the plasma column can be considered a 'consumable heating element' whose resistivity varies with operating conditions and type of gas used for ionization. The resistance range of a plasma in Ω cm is 0.01–0.5 for argon, 0.05–0.25 for nitrogen, and 0.25–0.0035 for hydrogen [17]. These values should be compared to the resistance ranges of solid materials such as iron (0.001–1.00), carbon (9×10^{-4}–3.5×10^{-3}) and copper (5×10^{-7}–9×10^{-8}).

An important design consideration for plasmatrons is the confinement of the plasma jet along the central channel of the torch by two phenomena, the thermal and the magnetic 'pinch'.

Thermal pinch occurs because at the cooled wall of the anode nozzle the conductivity of the gas is reduced thus increasing the current density at the centre. The

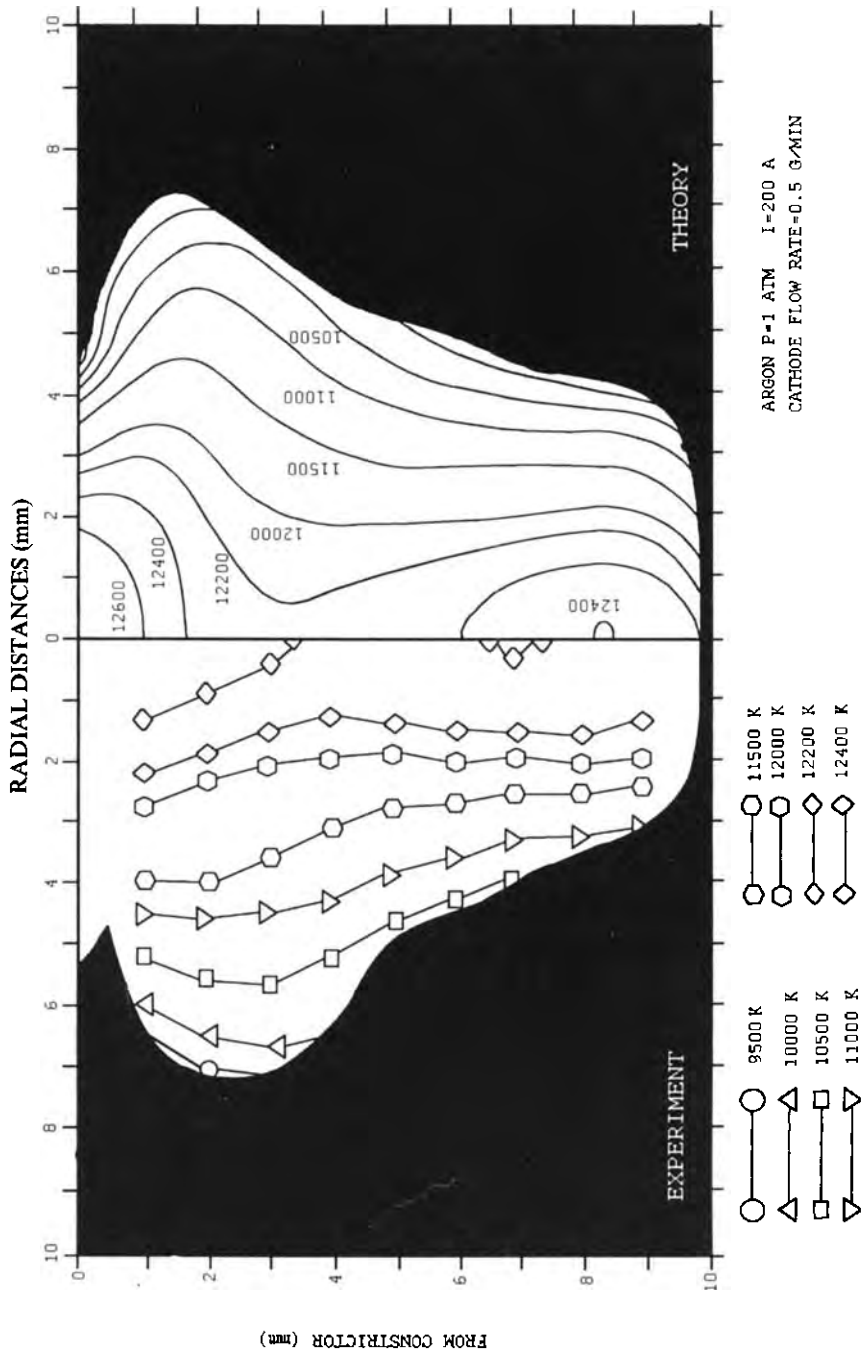

Figure 3-16. Anode region of a high intensity arc (after [16]).

charged plasma tends to concentrate along the torch axis thus confining the jet. Simply put, this means that the cold gas surrounding the arc absorbs a significant amount of energy from the arc in proportion to the energy required to ionize it.

Magnetic pinch is related to a magnetohydrodynamic Lorentz force created by the electrically conductive central region of the plasma jet. The moving charges induce a magnetic field. According to electrodynamics, the vector cross-product of the current and the magnetic field strength define the Lorentz force whose vector is mutually perpendicular to the former vectors. An inward moving force is created that constricts the jet even further. Its core pressure increases, and the jet is blown out of the front nozzle with supersonic speed.

Figure 3-17 shows schematically the direction of the Lorentz force $[\boldsymbol{j} \times \boldsymbol{B}]$ (longitudinal or z-pinch). The current flowing in the z-direction causes circular magnetic field lines $\boldsymbol{B}_\theta$ that compress and thus confine the plasma.

From the momentum conservation equation the Euler flow equation

$$\rho(\mathrm{d}\boldsymbol{v}/\mathrm{d}t) \equiv \rho(\mathrm{d}\boldsymbol{v}/\mathrm{d}t + (\boldsymbol{v}\nabla)\boldsymbol{v}) = (1/c)[\boldsymbol{j} \times \boldsymbol{B}] - \nabla p \tag{3-27}$$

can be derived, where $\rho(z, t)$ is the particle density, $\boldsymbol{v}(z, t)$ is the (macroscopic) particle flow velocity, p is the plasma pressure and $\rho(\boldsymbol{c}; \boldsymbol{c})$ is the tension tensor [2]. This equation neglects the influence of gravity and other volume forces such as centrifugal and Coriolis forces[3]. This leads to the simplified Navier–Stokes equation for momentum conservation,

$$\rho(\mathrm{d}\boldsymbol{v}/\mathrm{d}t) + \nabla p = [\boldsymbol{j} \times \boldsymbol{B}]. \tag{3-28}$$

The first term on the left side of the equation describes the time-dependent mass flux, i.e. the particle acceleration, the second term is the outward directed plasma pressure gradient. Their sum is balanced by the vector cross-product of the current and the magnetic field, i.e. the inwardly directed Lorentz force. For very high currents the z-pinch effect increases the temperature by magnetic compression considerably. Its value can be calculated by applying the Bennett equation

$$J^2 = 8\pi \mathrm{k} T n/\mu_0, \tag{3-29}$$

where n is the number of particles per unit length of the plasma cylinder, and μ_0 is the electron mobility. Plasma heating by magnetic compression is being utilized in nuclear fusion reactors.

3.3.1 Arc Discharge Generators and their Applications

There is a wide variety of approaches towards achieving high temperatures in a plasma jet heating device. Only a few basic principles will be considered here.

We can distinguish among three categories as shown in Table 3-2:

[3] However, it can be shown that a self-confinement of a finite plasma is impossible in a gravity-free environment by its own magnetic field alone [2].

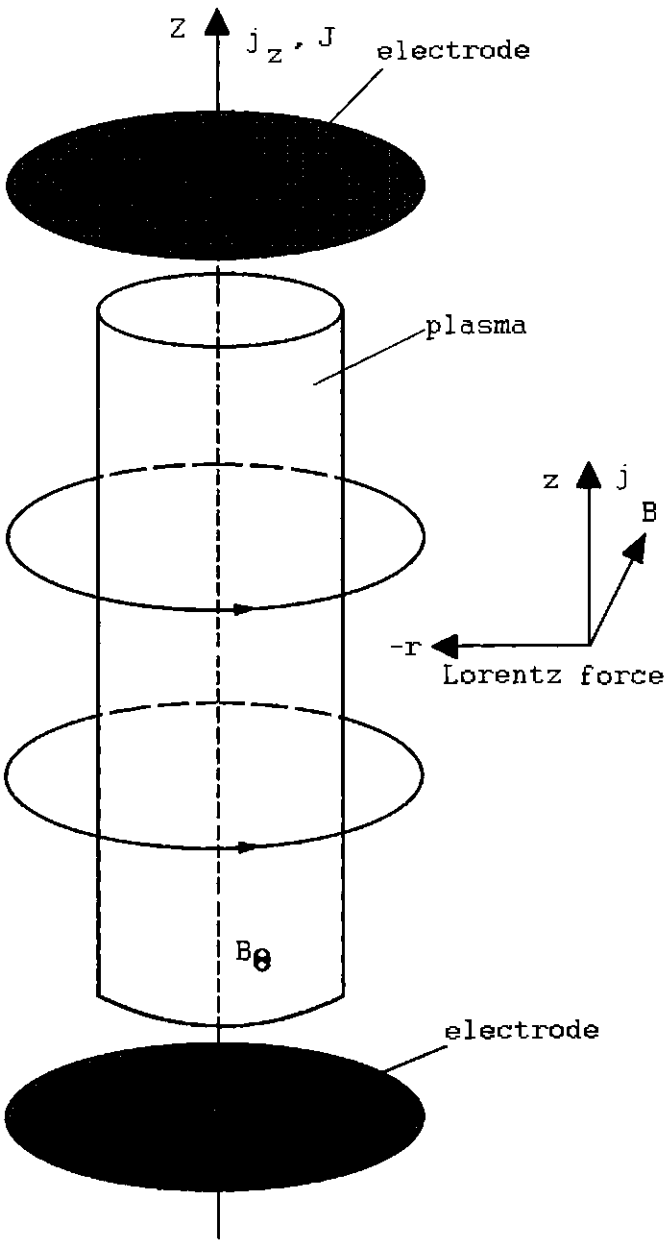

Figure 3-17. Direction of the Lorentz force (longitudinal or z-pinch).

Table 3-2. Arc discharge generators and uses: after reference [17].

Generators	Uses
Electrode plasmas (EPs)	
Nontransferred	
Low voltage	Spraying/particle heating
	Welding
	Melting
	Low velocity
	Gas heating
High voltage	High-pressure operation
	Hydrogen heating
	Spraying
Transferred	
Direct work heating	Welding
	Cutting
	Melting conductive materials
	Surfacing
Secondary Electrode	Spraying/particle heating
(Water stabilized, metal/carbon, multiple ring)	Gas heating
Electrodeless plasmas (ICPs)	
Low frequency	High power
	Gas heating
	Particle heating
High frequency	Low power
	Gas heating
	Particle heating
	Spraying
	High-resistivity gases
	High pressure
Hybrid	
ICPs superimposed on EPs	Particle heating
	Gas heating

d.c. types: wall/gas/magnetically stabilized, pin/hollow electrodes, fixed/movable electrodes, external field augmentation; a.c. types: single- and multiphase, fixed/movable electrodes, external magnetic field augmentation; electrodeless types: tandem inductive coupling, tandem capacitive coupling, inductive/capacitive coupling.

- electrode plasmas (EP) as either nontransferred or transferred plasmas,
- electrodeless plasmas (inductively coupled plasmas, ICP) operating at low or high frequencies, and
- hybrid devices where ICPs are superimposed on EPs [17].

3.3.1.1 Electrode-supported Plasmas

Nontransferred electrode plasmatrons (*indirect plasmatrons*) operate at comparatively low voltages between 20 and 150 V d.c. Figure 3-18 shows the cross-section of a typ-

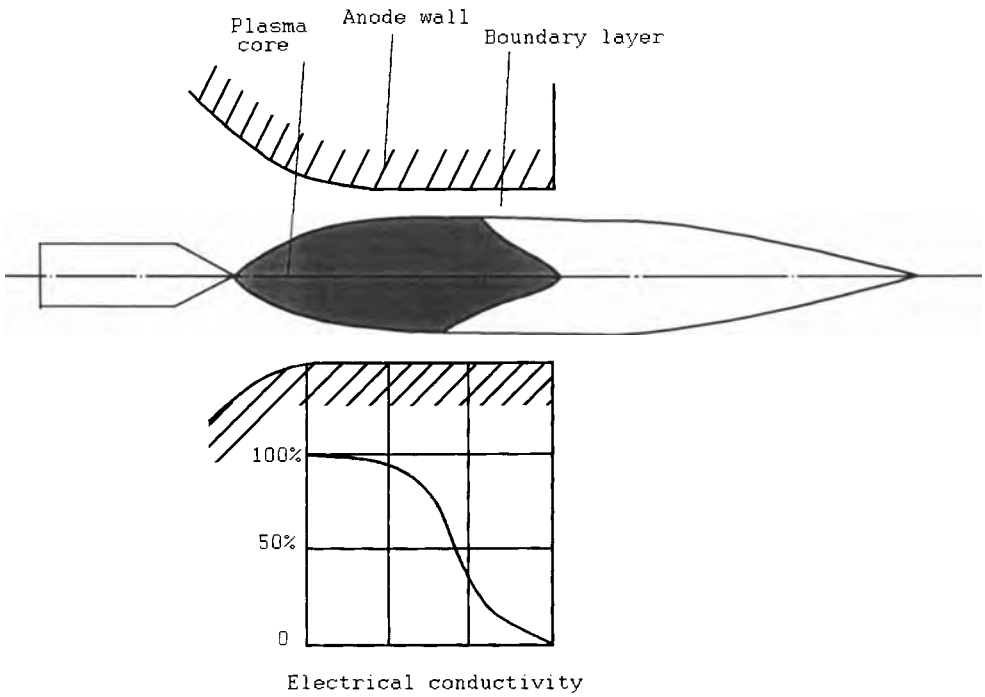

Figure 3-18. Cross-section of a typical nontransferred d.c. plasmatron.

ical nontransferred d.c. plasmatron. It consists of a stick- or bullet-shaped cathode made from tungsten, and a water-cooled copper anode which forms the front nozzle of the torch. The tungsten cathode is thoriated to lower the electron work function, and to get an abundance of electron emissions that initiate and sustain an electric arc between the tip of the cathode and the internal diameter of the positive anode nozzle. The plasma rapidly diminishes in charged particle density near the nozzle exit. This results in an exponential decrease in electrical conductivity as shown in the lower part of Fig. 3-18. The actual discharge is initiated by a high frequency pulse or a high voltage field emission discharge. The arc stretches down the cathode with a constant voltage gradient and is attached to the anode by a voltage drop (anode fall). The flow through the torch is mildly turbulent with a miniumum swirl content for devices operated at low voltages. High voltages between 150 and 1 000 V, however show a significant amount of highly turbulent swirl gas that produces a strong vortex with a low-pressure center core that must be traveled through by the arc.

The heat transfer rates are close to the heat flux failure limit of the anode, i.e. copper material [17]. Therefore, effective cooling by a constant stream of water is essential to keep the anode from evaporating. In this configuration the maximum cathode amperage is about 3 000 A. This sets a maximum achievable power. For example, at a voltage of 200 V the maximum electrical power input would be 600 kW. The workpiece to be coated remains relatively cool and rarely exceeds 200 °C.

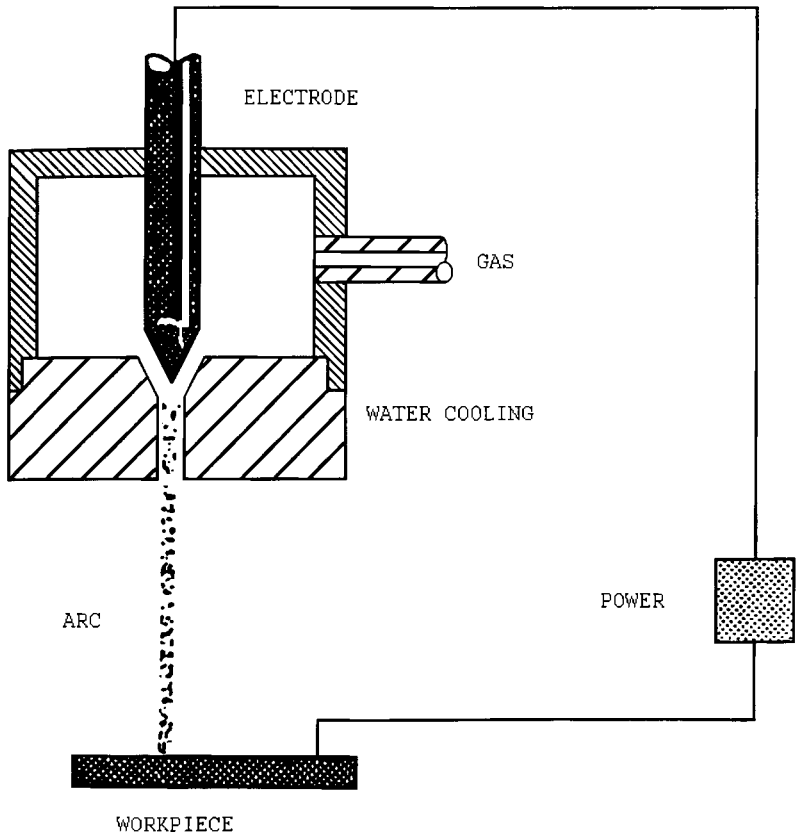

Figure 3-19. Working principle of a direct plasmatron (transferred electrode plasmatron).

Transferred electrode plasmatrons (*direct plasmatrons*) can be operated in two modes: transfer of energy to the workpiece that is electrically connected to the power source, and transfer of energy to an intermediate electrode.

In the first type (Fig. 3-19), the cathode is some distance (usually less than 15 cm) from the 'working' anode. An arc is struck between the two electrodes by either a capacitance or a high-frequency discharge with the direct current following the ionized path thus generated. The workpiece (substrate) is electrically connected to the power source, and the whole assembly actually constitutes an arc-welding configuration. This means that the substrate is heated to high temperatures. The heat losses by radiation or convection are high (20–40%). If the system is used for plasma spraying, care must be taken to inject the powder downstream of the arc root at the anode to avoid contamination of the electrodes. Also, the substrate may have to be cooled in order to avoid melting, warping or undesirable changes of the microstructure.

Applications of a transferred arc include welding, cutting and melting operations of conductive materials. With severe constriction of the arc by an intermediate nozzle of small diameter, the heat flux and gas velocity are very high, and this device is

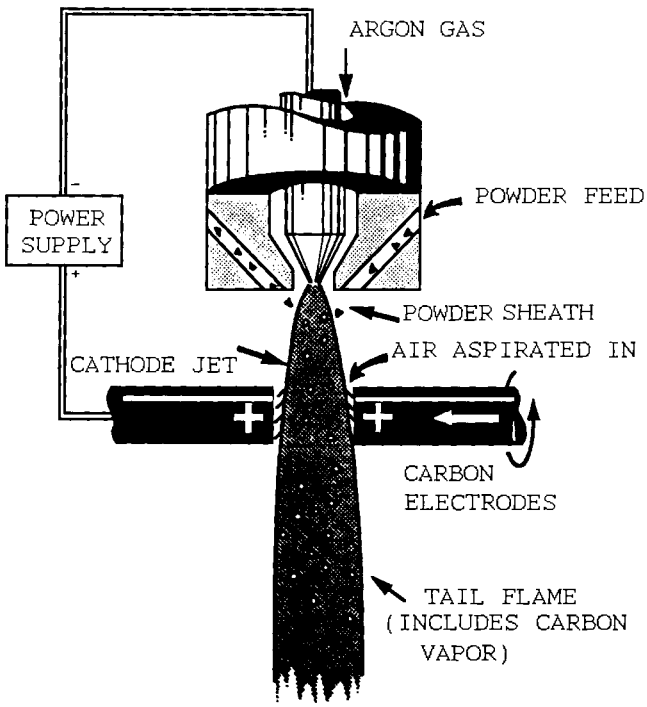

Figure 3-20. Working principle of a transferred arc terminated by an intermediate electrode [17].

therefore used for cutting metal. Less constricted arcs with larger intermediate nozzle size have lower gas velocities. Thus the arc is 'softer' and can be used for welding and melting operations.

In the second type (Fig. 3-20), the transferred arc is terminated by an intermediate electrode that produces a nontransferred free plasma jet. As shown in the figure, the secondary carbon anode is self-cleaning and slowly consumed. In the Ionarc (TAFA Inc., Concord, NH, USA) device shown there are three rotating carbon electrodes that are fed at a rate that replenishes the consumed material. Powder injected close to the cathode spot can be heated with high thermal efficiency. For example, the powder feed rate is as high as $0.9\,\mathrm{kg\,h^{-1}\,kW^{-1}}$ as opposed to $0.1\,\mathrm{kg\,h^{-1}\,kW^{-1}}$ for normal tail-flame injection type plasmatrons.

Today, transferred arcs are frequently used to clean the surface of the part to be coated by sputtering off oxide scale. This requires a polarity change, i.e. the working anode is made more negative for some time. This procedure is particularly important if highly oxygen-sensitive material is to be sprayed in a 'vacuum' environment, such as NiCrAlY for coating of gas turbine vanes and blades for aerospace applications.

Segmented anodes allow the arc to strike from the central cathode through one or more insulated and water-cooled metal rings to the terminating, also water-cooled anode rings (Fig. 3-21a). This is done to increase the arc voltage that permits higher power operation. Since the amperage is reduced at given power level electrode life is increased because erosion is decreased.

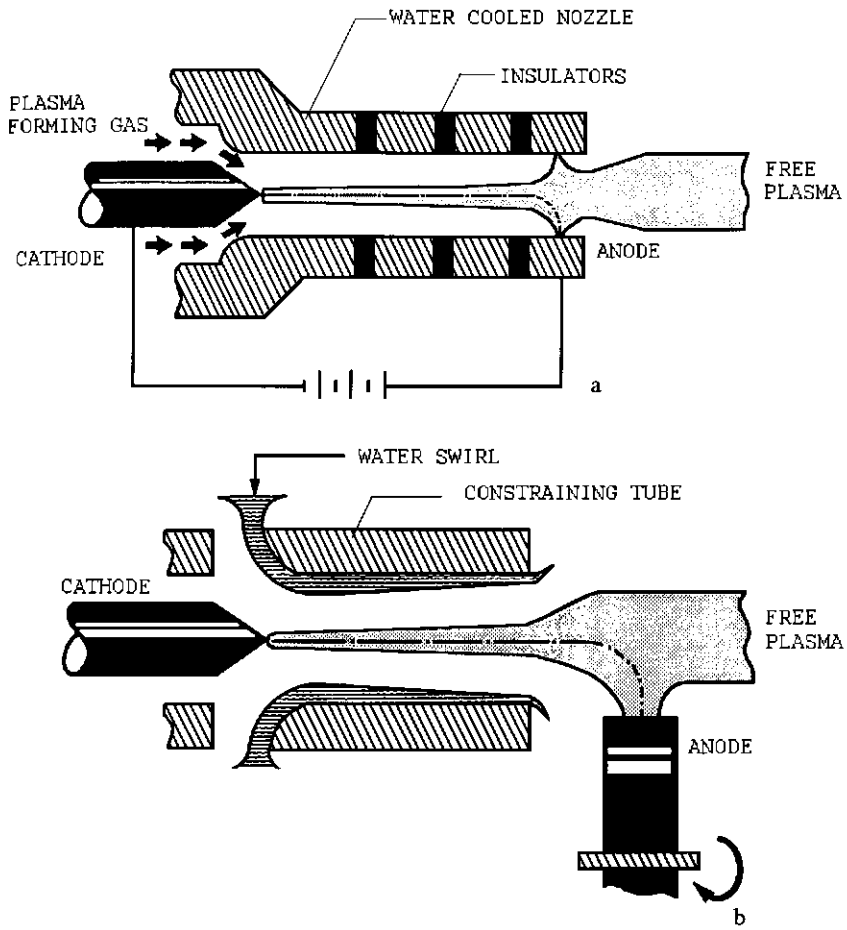

Figure 3-21. Segmented anode plasma (a) and water-stabilized arc (b) [17].

Figure 3-21b shows a water-stabilized arc (see Sec. 3.3.2.2). Water vortices in a tube section between consumable cathode and anode form a hollow passage and protect the walls from overheating. Very high power can be applied and temperatures can therefore reach 50 000 K (Gerdien arc, [18]). Transferred water-stabilized arcs are being used to spray alumina at powder feed rates as high as 34 kg h^{-1} compared with less than 10 kg h^{-1} for a conventional gas-stabilized nontransferred d.c. arc [17].

3.3.1.2 Electrodeless Plasmas

Radiofrequency (RF) inductively-coupled Plasma (ICP) devices were conceived by Reed in 1961 [19], and treated extensively theoretically, for example by Eckert [20] and Boulos [21]. They generally consist of a coil surrounding a water or gas-cooled refractory (often silica glass) tube through which the plasma-forming gas, the sheath-

gas for wall cooling, and the powder gas pass (Fig. 3-22). The devices operate in widely varying power (0.5 kW–1.0 MW) and frequency (9.6 kHz–40 MHz) ranges [21].

Energy coupling to the plasma is achieved through the electromagnetic field of an induction coil. The plasma gases do not come in contact with any electrode and therefore any contamination is largely excluded. Mostly argon is used because of its ease of ionization. The device, however, works also well with an air plasma.

The main attraction of the radio-frequency inductively coupled torch is in-flight melting of relatively large particles of refractory metals and ceramic powders at high throughputs.

Figure 3-22 shows schematically the temperature (left) and flow fields (right) in the discharge region of an inductively coupled torch [21, 22]. The maximum plasma temperature is off-axis because the energy dissipation is limited to the outer annular region of the discharge. The argon plasma (power level 3 kW, oscillator frequency 3 MHz) is confined in a water-cooled silica glass tube with several gaseous stream introduced. Q_1 ($=3\,\mathrm{l\,min^{-1}}$) is the axially injected powder gas that serves to introduce the material into the plasma, Q_2 is the intermediate gas that serves to stabilize the plasma and is kept constant at $3\,\mathrm{l\,min^{-1}}$; it is often introduced with both axial and tangential velocity components. Q_3 is the sheath gas that serves to reduce the heat flux to the walls of the confinement tube, and thus protects it from damage due to overheating. In this example it had been adjusted in such a way that the total flow rate Q_0 is constant at $20\,\mathrm{l\,min^{-1}}$.

The flow field shows low velocities ($10–20\,\mathrm{m\,s^{-1}}$) compared to a d.c. plasma arc torch ($100–400\,\mathrm{m\,s^{-1}}$). There exists an recirculation eddy current in the coil region, caused by the electromagnetic pinch effect. In order to properly deliver the powder into the torch, it has either to be introduced at high velocity to overcome the back flow, or to be injected in the middle of the induction coil region, below the recirculation eddy current.

Advantages of this method include:

- no electrodes,
- any gas possible,
- no upper temperature limit,
- low velocity plasma,
- large diameter plasmas,
- quasi-laminar flow regime, i.e. low Reynolds numbers, and
- operational without gas flow because of arc stabilization by thermal pinch in the center of the tube.

Disadvantages include:

- high frequencies and voltages that lead to high transmission losses,
- low power densities, and thus lower maximum temperatures (usually below 10 000 K),
- local cooling of plasma at point of powder injection, and
- complex geometry of device that makes fixation necessary.

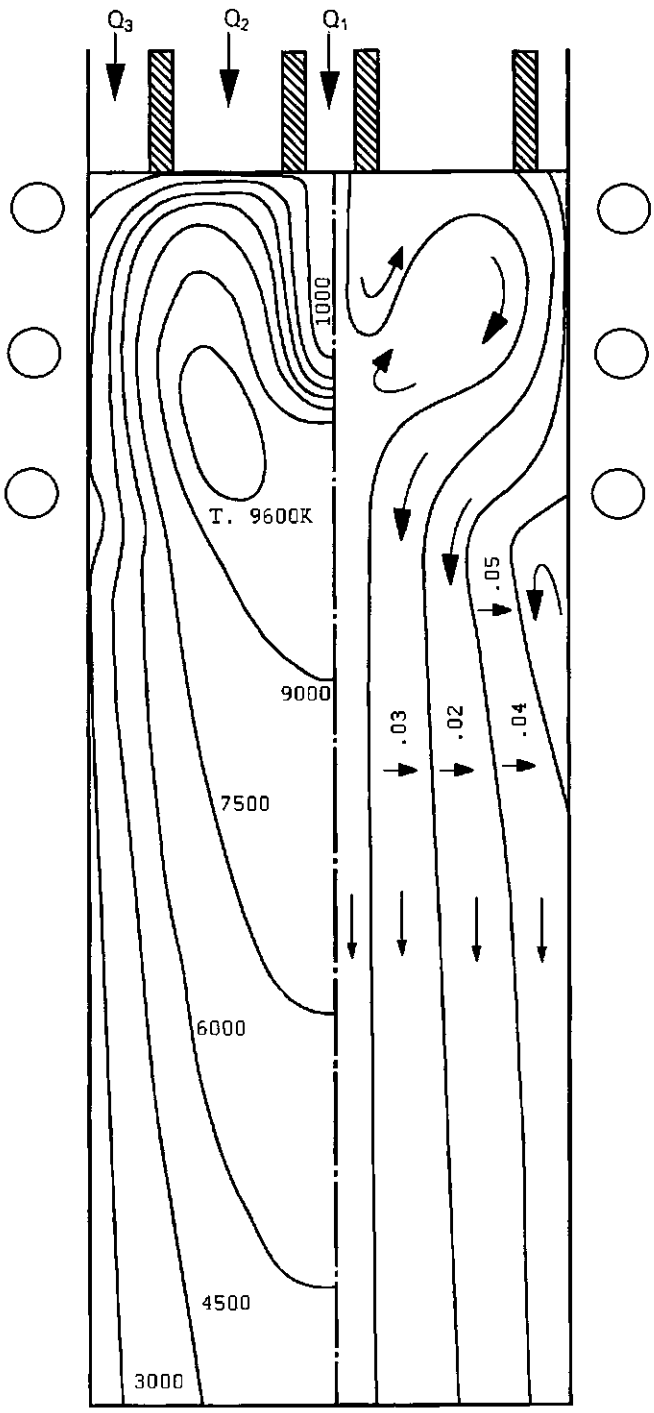

Figure 3-22. Electrodeless radiofrequency inductively-coupled plasmatron. Left section: temperature distribution. Right section: flow field distribution [21].

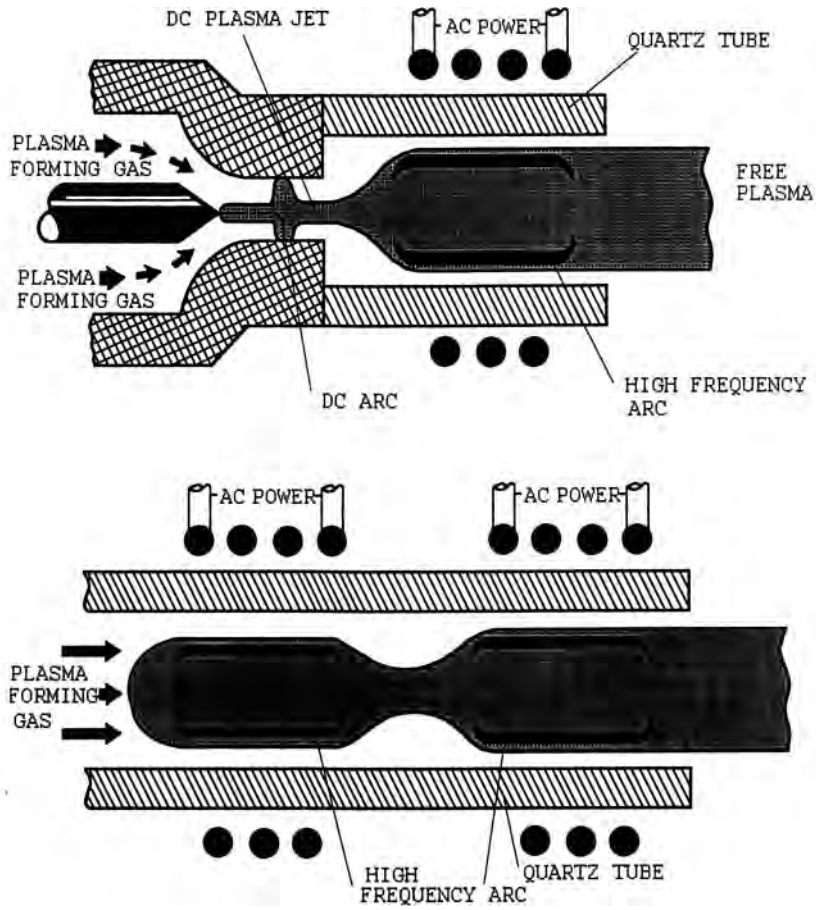

Figure 3-23. Inductively-coupled plasmatron (ICP) operated in tandem with another ICP (bottom) or a d.c. discharge (top) [17].

3.3.1.3 Hybrid Devices

It is feasible to operate the ICP in tandem with either another IPC (Fig. 3-23, bottom) or a d.c. discharge (Fig. 3-23, top). The d.c. plasma forms the center core of the plasma, acting as an ignition source, and the ICP adds additional heat downstream to maintain the temperature level. It also increases the diameter of the plasma, i.e. the volume of the plasma and its energy density so that more powder per unit time can be processed by the device. There are, however, problems with plasma contamination by the material evaporated from the d.c. plasmatron electrodes. The lengthening of the plasma zone by several hybrid devices is shown in Fig. 3-24. It provides the possibility to achieve higher particles residence time in the hot zone, and also adds design flexibility when chemical reaction times have to be increased, for example in reactive plasma processing [23]. Successful approaches to hybrid devices

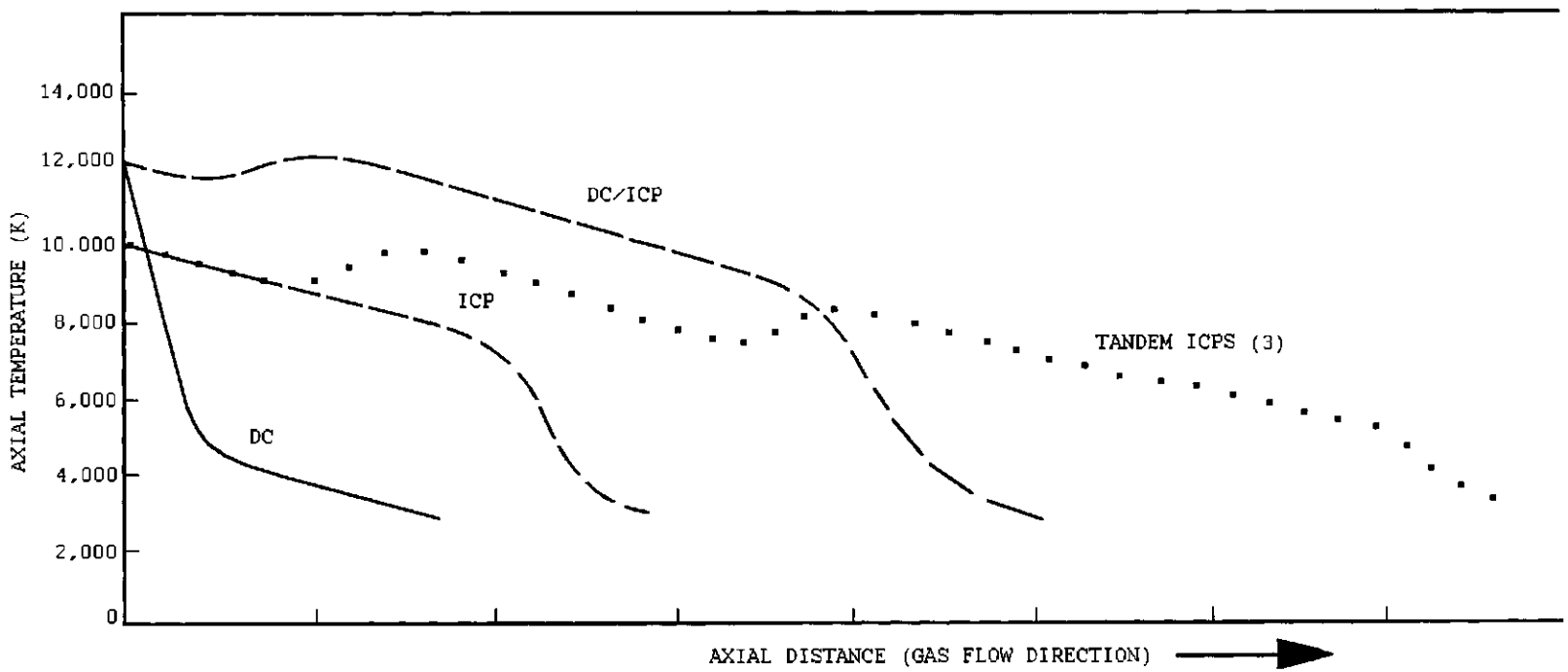

Figure 3-24. Axial temperature variations of d.c., ICP, and tandem-operated d.c./ICP and ICP/ICP plasmatrons [17].

were taken by Yoshida *et al.* [24] using a d.c. power of 4–5 kW, an RF plate power of 10–30 kW, and an oscillation frequency of 4 MHz, and by Takeyama and Fukuda [25] using an RF–RF two frequency hybrid plasma (pilot RF source with 2 kW and 27.12 MHz, and secondary RF source with 15 kW at 5 MHz).

3.3.2 Stabilization of Plasma Arcs

Since the power supply of the plasmatron normally has a negative characteristic ($R = \mathrm{d}V/\mathrm{d}I < 0$), it is inherently unstable. The voltage decreases with increasing current so that for steady-state conditions a resistance must be included in the circuit. The slope of the load line is given by $\mathrm{d}v/\mathrm{d}i = -R$. The intersections of the characteristics (load line) of the current source and the plasmatron define the two stable working points A and B of the device. The Kaufman stability criterion of a plasmatron is $\mathrm{d}v/\mathrm{d}i + R > 0$ or $R > |\mathrm{d}v/\mathrm{d}i|$. Considering the capacitance and inductance of the arc, the criterion becomes $R < L/c|\mathrm{d}v/\mathrm{d}i|$.

Electric stabilization can be achieved in several ways:

- power supply with a rectifier with a saturable core,
- thyristor-controlled silicon rectifier system and inductor to damp high frequency transient current variations leading to erratic movement of the arc root at the anode surface,
- additive stabilization resistance of the electric cables in the water-cooled circuits of the torch,
- several gas- or liquid-stabilized arc configurations.

3.3.2.1 Wall-stabilized Arcs

Wall-stabilized designs consist of a solid and a hollow electrode, and the plasma gas, instead of constricting the arc, becomes an integral part of it, filling the nozzle from wall to wall. Since for a cylindrical symmetric arc with fixed temperature boundary and therefore predominant thermal conduction losses the whole discharge is determined for a given current I, the field strength is determined almost entirely by R (thus $E \propto 1/R$), and the axial temperature T_0 increases with the input power per unit length, EI. Since with forced cooling the effective wall radius decreases, for a given current EI and T_0 increase. This explains the apparent anomaly that with enhanced cooling the temperature increases.

3.3.2.2 Convection-stabilized Arcs

In the wall-stabilized arc the discharge fills the major portion of the internal nozzle tube space, and for large nozzle diameters the arc can be wall-stabilized only if very high currents and arc temperatures exist. The large tube constitutes essentially the condition of a free-burning arc that requires no external stabilization at low currents.

Stabilization in this case is achieved by convective gas flow. The energy equation consists of a conductive and a convective term:

$$\sigma E^2 = \nabla(-k\nabla T) + \rho v_0(C_p \nabla T + \nabla\Phi), \tag{3-30}$$

where C_p is the specific heat at constant pressure, k is the thermal conductivity of the plasma gas, and v_0 is the volume of the tube space. The convective term makes it possible for arc stabilization to occur without the maintenance of thermal conduction to the wall boundaries. In the outer regions of a cylindrically symmetric arc the energy flow is constant and equals the total energy input, E, but the balance between the conductive and convective terms changes as the radius increases. Ultimately, before the wall boundaries are reached, the convective term predominates the conductive term, and the thermal conduction becomes negligible. The convective gas thus acts effectively as a boundary wall and the arc is convection-stabilized. From Eq. 3-30 it can be gathered that energy is transported by mass flow only when the flow has a component in the direction of the temperature or gravity gradient. In a *vertical arc* a steady-state is established between the forces of gravity and viscosity, and the gas moving upward flows into the lower arc portion thus cooling this region. When leaving the upper arc region, however, the flow heats the arc since the flow is against the temperature gradient. Thus convection tends to broaden a vertical arc at the top. In the case of a *horizontal arc* a similar process occurs where convection produces arc bowing [26].

In the *vortex stabilized arc*, the electrodes are made from tungsten, carbon or other materials, and may be water-cooled. Gas is fed tangentially into the chamber between the electrodes to produce an intense vortex within the hollow electrode, which usually is the cathode. Thus, the arc is forced to travel from the solid anode out of the nozzle and then strike back to the front face on the hollow cathode. Since the arc channel is imbedded in the vortex flow intense convective cooling of the arc fringes occurs. The media producing the vortex can be liquids (water; Gerdien arc [18]) or gases (high field-strength hydrogen arc). Modified arrangements of vortex-stabilized arcs rely on a rotating discharge vessel ('Wälzbogen') or a torus stabilized by a toroidal vortex [3]. In some plasma reactors to synthesize ultrafine particles an argon gas shroud is used to convection-stabilize the plasma arc [27].

3.3.2.3 Electrode-stabilized Arcs

When the electrode separation is small (1 mm) and the electrode mass is large, it is possible for the arc to be dominated and thus stabilized by the energy losses to the electrodes. In this case the electric field and current distribution may be symmetric about the midplane of the electrode system [26]. The arc contour is elliptic with the electrodes acting as focal points.

3.3.2.4 Other Stabilization Methods

The *gas-sheath stabilized plasma jet* is between a solid tungsten cathode and a hollow water-cooled copper anode. The arc remains within the nozzle and is prevented from

striking the wall by a gas sheath that is much thicker than the arc diameter. Vortex flow is not used, and the position of the arc is determined by the gas flow pattern and the turbulences.

In a *magnetically-stabilized jet*, the arc strikes radially from an inner to an outer electrode. Gas is blown axially through the annulus. The arc is rapidly rotated by a magnetic field, so that its position at various times resembles the spokes of a wheel. With this design, high pressure jets can be created without erosion of the electrodes. Since the external magnetic field interacts with the charged particles in the plasma the arc is magnetically stabilized in a cross-flow: the drag force acting on the arc is effectively compensated by the Lorentz force ($\boldsymbol{j} \times \boldsymbol{B} \propto C_D^2$), and the arc actually behaves similarly to a solid body with respect to its response to drag. The arc cross-section assumes the shape of an ellipse with its major axis perpendicular to the jet axis. Within this elliptic contour two symmetric vortices with opposite directions of rotation are formed. Magnetically-stabilized arcs are extensively used for applications in arc gas heaters including plasmatrons, circuit breakers, arc furnaces, arc welding devices, and plasma propulsion systems.

3.3.3 Temperature and Velocity Distribution in a Plasma Jet

3.3.3.1 Turbulent Jets

The complex magnetohydrodynamic interactions within a plasma jet affect profoundly the macroscopic plasma parameters temperature and velocity. There exist strong temperature and plasma velocity gradients in a plasma arc jet. Figure 3-25 shows the temperature (a) and the axial velocity v_z (b) of a typical d.c. argon/hydrogen arc along the direction of propagation of the plasma jet, z [28]. The isotherms show clearly that the maximum temperature exists in the core of the jet close to the nozzle exit ($z = 0$) and the center line ($r = 0$). This very hot region is followed by a transitional region in which the plasma temperature falls rapidly to less than 3 000 K at $z = 80$ mm. Eventually there is the fully developed region in which the gas temperature decreases rather gradually by mixing with entrained cold ambient air. The radial temperature profile is extremely steep in the core region with temperature gradients of more than 4 000 K over the distance $r = 1$ mm. It is this very steep temperature gradient that makes difficult the problem of complete heating of the powder particles (see Chap. 4) and thus necessitates close control of particle size distribution and injection conditions into the plasma jet. The extremely large radial and axial temperature gradients require that in order to properly melt them, the injected particles should travel close to the center line. Also, the axial velocity isopleths indicate a fast velocity decay away from the point of injection close to the nozzle exit. To measure the velocity of the plasma, small amounts of fine alumina particles (3 μm diameter) were injected as tracers under the assumption that they do not influence the flow conditions and the temperature field. The radial velocity distribution at $z = 5$ mm in an atmospheric argon jet is shown in Fig. 3-26 for an arc current of 286 A. Figure 3-27 shows the associated radial temperature distributions at $z = 5$ mm for different currents ranging from 147 to 268 A. The tracer particles were injected at a rate of $0.18\,\mathrm{g\,s^{-1}}$. Figure 3-28 finally indicates the symmetric enthaly distri-

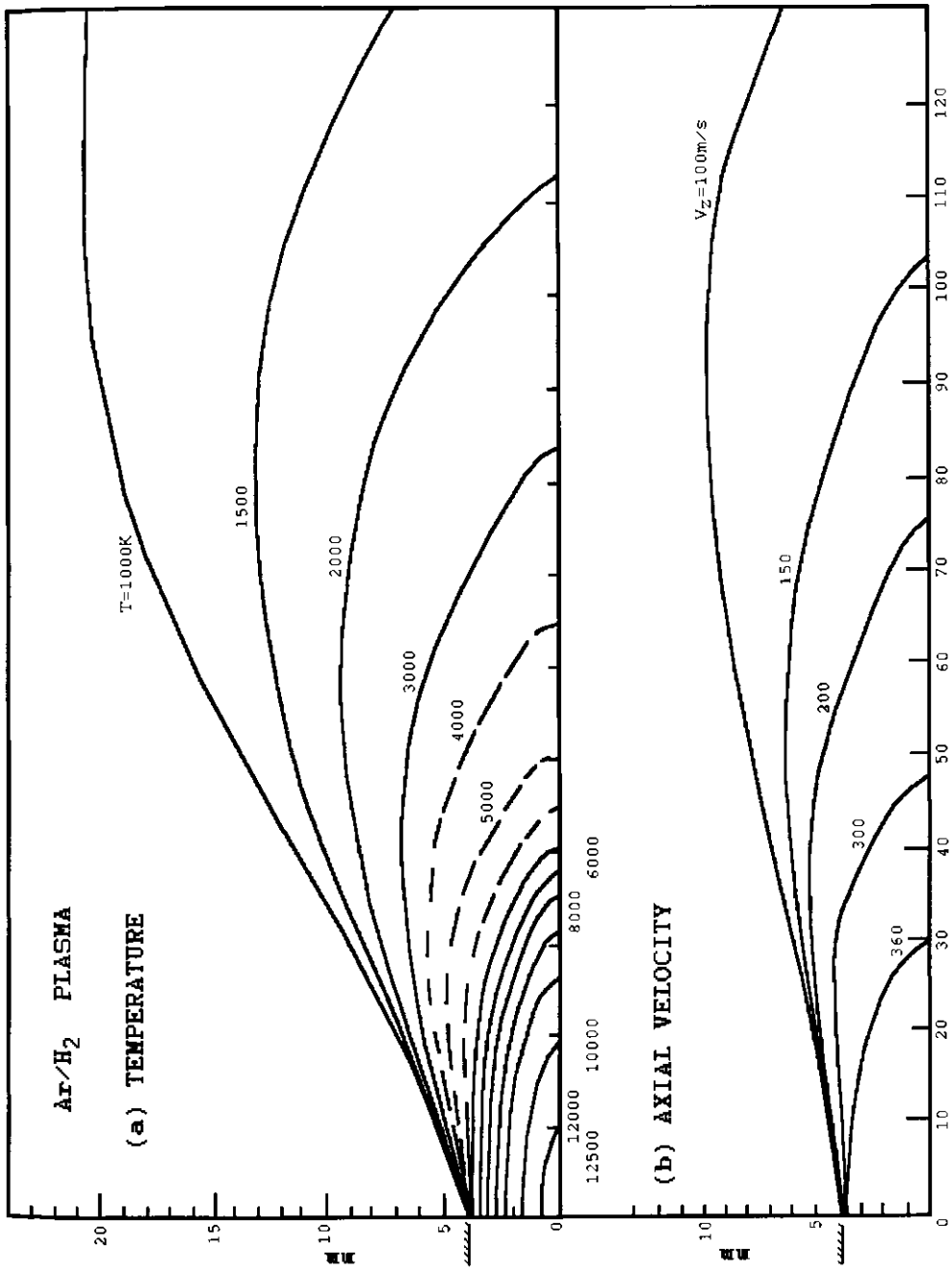

Figure 3-25. Temperature (a) and axial velocity (b) distribution of a typical d.c. argon/hydrogen plasma arc along the direction of propagation, z [28].

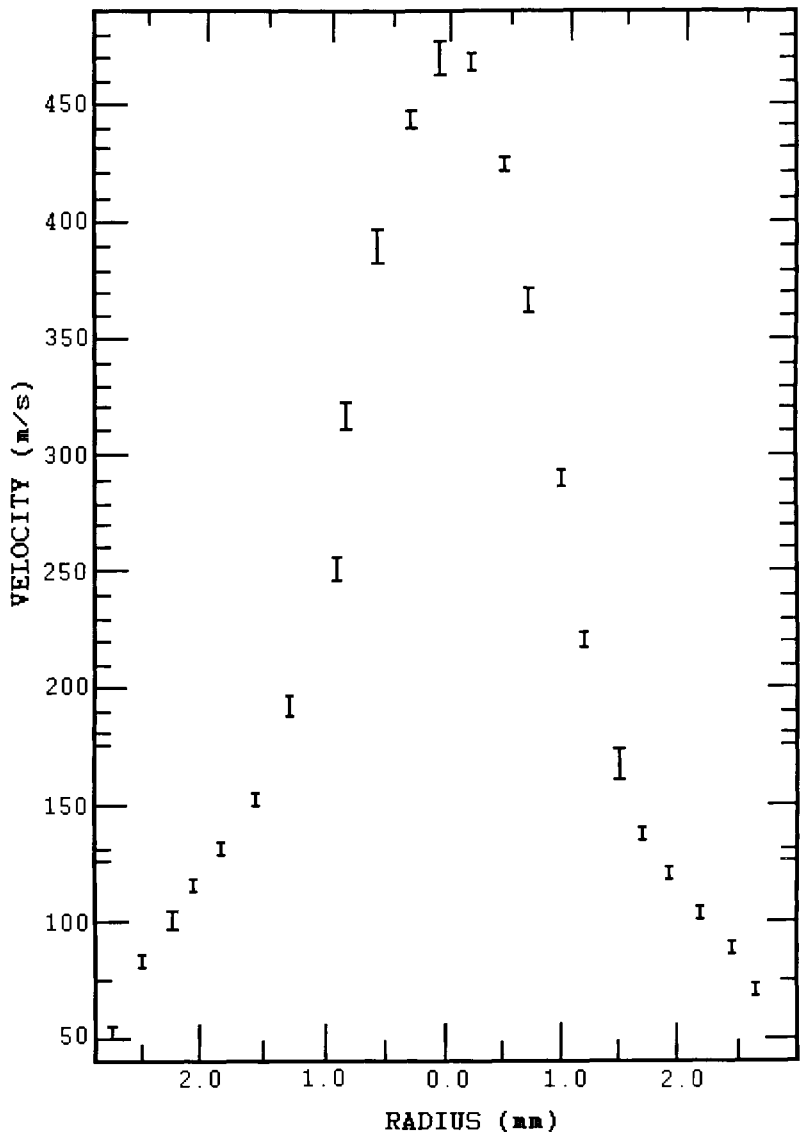

Figure 3-26. Radial velocity distribution at $z = 5$ mm in an atmospheric argon plasma jet at an arc current of 286 A [29].

bution in kJ kg^{-1} [29]. Temperatures, velocities and enthalpies can be measured with sophisticated probing techniques (for details see Sec. 3.4).

The symmetry of the distributions shown in Figs 3-25 to 3-28 suggests the picture of a quiet, undisturbed and essentially laminar flow within the plasma column. This, however, is far from reality. As the gas flow increases as required in energy-efficient high temperature plasmatrons, large scale flow structures evolve that are dominated by turbulences and entrained eddies of cold surrounding air. In particular, the large

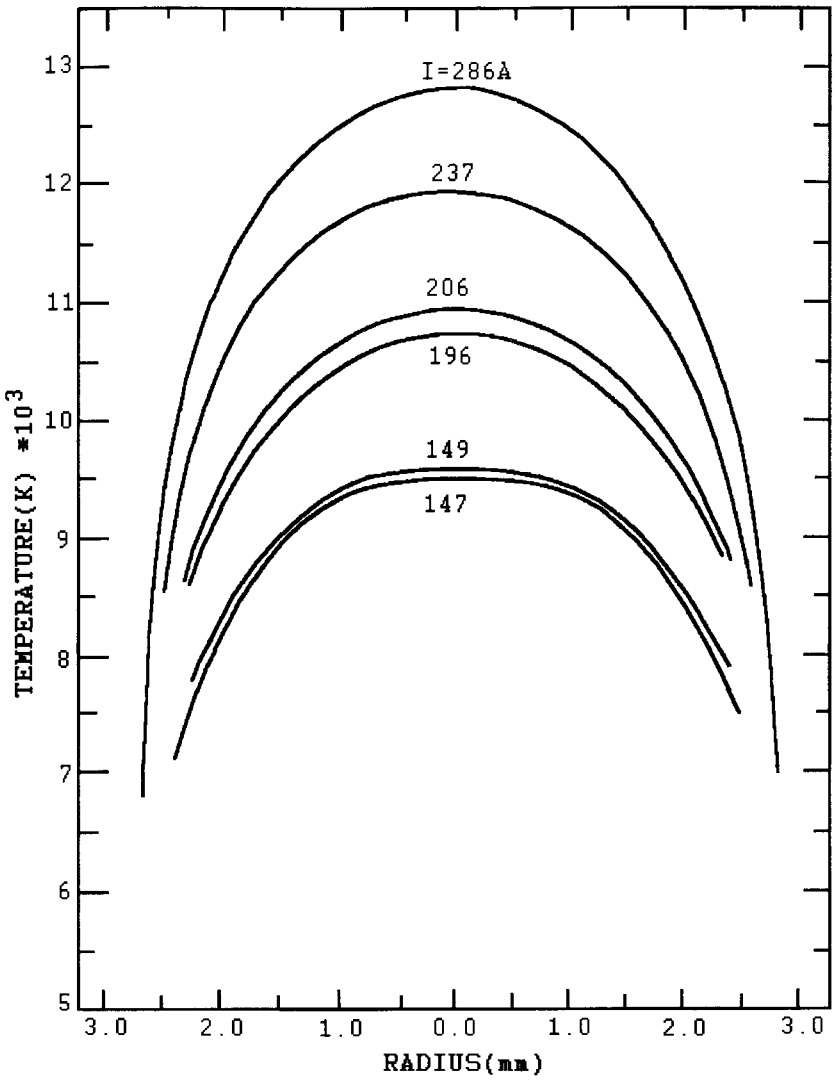

Figure 3-27. Radial temperature distribution at $z = 5$ mm in an atmospheric argon plasma jet at various currents [29].

difference in density of the plasma gas and the atmospheric air increases the degree of turbulence. Figure 3-29 shows the complex structure of a plasma jet approaching transition from a laminar to a fully turbulent flow regime. Following Pfender *et al.* [30], the plasma jet leaving the nozzle encounters a steep laminar shear at the jet's outer edge that causes a rolling-up of the flow around the nozzel into a ring vortex. This vortex is pulled downstream by the gas flow, and allows thus the process of ring vortex formation to continue. The subsequently formed rings have the tendency to coalesce forming larger vortices. Perturbations of the latter lead to wave instabilities.

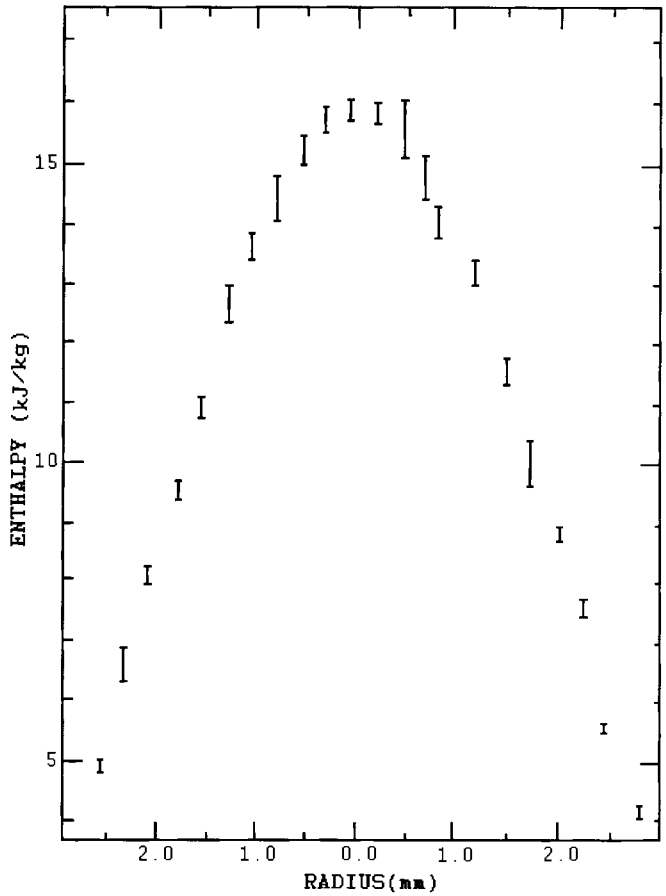

Figure 3.28. Enthalpy distribution at $z = 5$ mm in an argon plasma jet at 286 A [29].

Finally, the vortex interactions result in a total breakdown of the vortex structure into large scale eddies and the onset of turbulent flow[4]. Since the entrained eddies of cold air have a density and inertia much higher than that of the high temperature plasma gas, the cool eddies are left behind when the hot plasma gas is accelerated around them. Thus initally little mixing occurs. With increasing distance from the nozzle exit, however, the larger eddies are breaking down into smaller and smaller ones, and mixing and diffusion at the eddy boundaries increase. Eventually the mixing process reaches the center line of the jet, and destroys the plasma core. At this point the jet undergoes the transition to a fully turbulent flow regime. As a result, both the temperature and the velocity of the jet decay. The consequences of this process for the melting behavior of injected powder particles will be explored in Chap. 4.

[4] This have been humorously described, in verse, by Lewis F. Richardson [31]: 'Big whorls have little whorls/Which feed on their velocity,/And little whorls have lesser whorls/An so on to viscosity'. This is a take-off on the well-known verse by Jonathan Swift: 'So, naturalists observe, a flea/Hath smaller fleas that on him prey;/And these have smaller fleas to bite 'em,/And so proceed *ad infinitum*.'

3.3.3.2 Quasi-laminar Jets

To modify the tubulent d.c. plasma jet towards quasi-laminar flow condition a so-called Laval nozzle is attached to the front of the anode (Fig. 3-30). The powder is injected within this nozzle at different ports whose positions depend on the melting

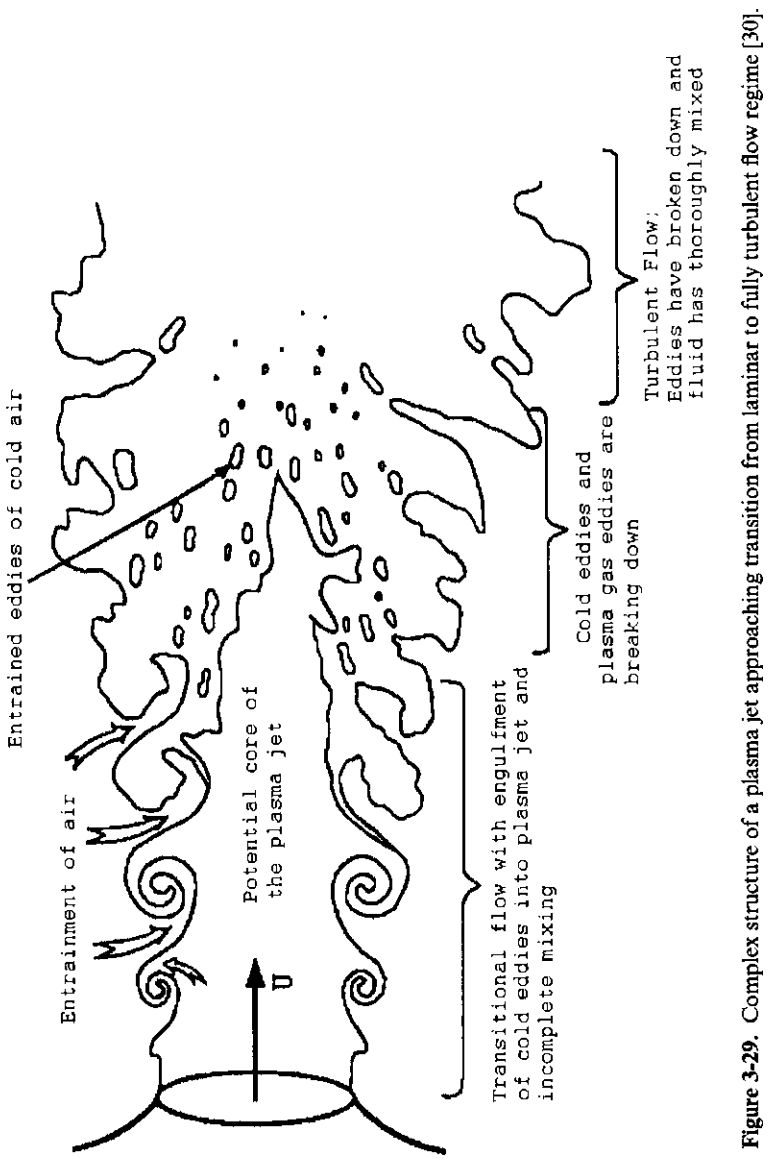

Figure 3-29. Complex structure of a plasma jet approaching transition from laminar to fully turbulent flow regime [30].

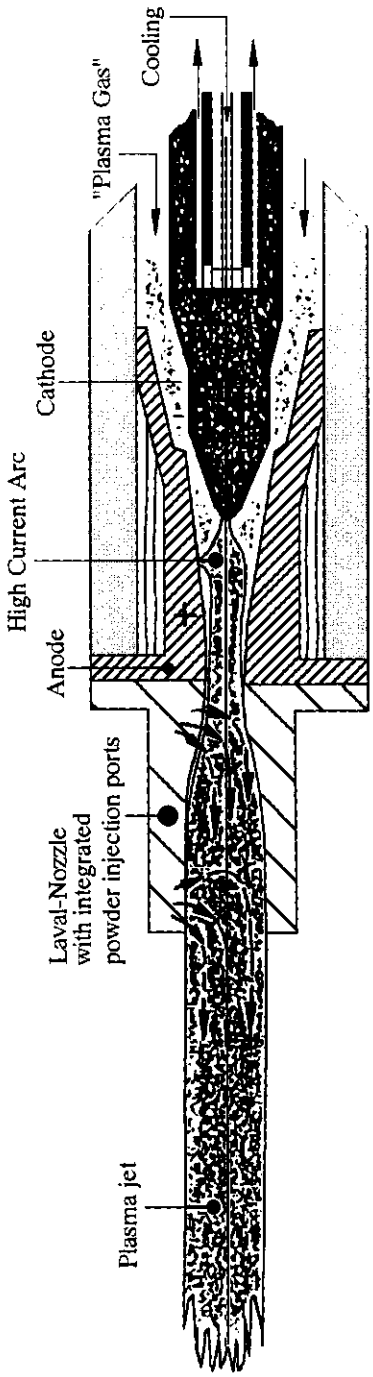

Figure 3-30. Principle of the DLR-VPS plasmatron with attached Laval nozzle and integrated injection ports (DLR: Deutsche Forschungsgesellschaft für Luft- und Raumfahrt) [32].

temperature of the material to be plasma-sprayed. One port is located close to the nozzle root where dense, hot and relatively slow plasma conditions prevail that aid in effective melting of materials with high melting temperatures. The other port is close to the nozzle exit [32]. Owing to the special layout of the inner nozzle contour [33] a long quasi-laminar plasma jet is produced that reduces the reaction between spray powder and surrounding residual oxygen by essentially two mechanisms. First, the residence time of the particles in the jet is strongly reduced (< 1 ms for alumina particles $-22 + 5.6\,\mu m$) since the plasma jet acquires a velocity of $> 800\,m\,s^{-1}$ (50 mbar chamber pressure, 600 A, 6 V, Ar/H_2 @ 60/5 SLMP (Standard liter per minute)) [32]. Second, because of the laminar characteristics of the plasma jet the powder particles are carried close to the central jet axis so that their divergence is low. Consequently, the particles have a lesser chance of reacting with residual oxygen surrounding the jet and being entrained by the remaining turbulent eddies. Thus the level of impurities within the deposited coating can be better controlled. This low divergence ($> 60\%$ of the particles are deposited within a circle of 20 mm diameter at a stand-off distance of 300 mm) leads naturally to an improved deposition efficiency and thus to a more economical operation of the plasmatron.

3.4 Plasma Diagnostics: Temperature, Enthalpy and Velocity Measurements

Vardelle *et al.* [34] developed a highly sophisticated system to measure, simultaneously, plasma temperature field, plasma velocity field, particle number flux, particle velocity distribution, and particle temperature distribution. Figure 3-31 shows the equipment. Before discussing the details of the results of these measurements, the physical background of the diagnostic methods will be briefly reviewed. In this chapter, only plasma diagnostics, i.e. plasma temperature and velocity field measurments will be covered. Particle diagnostics will be treated in Chap. 4.

3.4.1 Temperature Measurements

3.4.1.1 Spectroscopic Methods

In the plasma jet with temperatures approaching 15 000 K conventional temperature measuring techniques are unsuccessful. Plasma temperatures can be measured assuming local thermodynamic equilibrium (LTE) using atomic or molecular spectroscopy. These methods have the advantage of high spatial resolution but can be applied only if the temperatures exceed about 6 000 K. The plasma temperature field can be approximately deduced from the volumetric emission coefficient $\varepsilon_L(r)$ of suitable atomic emission lines, such as N I (746.8 nm) for a nitrogen plasma, and Ar I (763.5 nm) or Ar II (480.6 nm) for an argon plasma. The local emissivity ε_L is

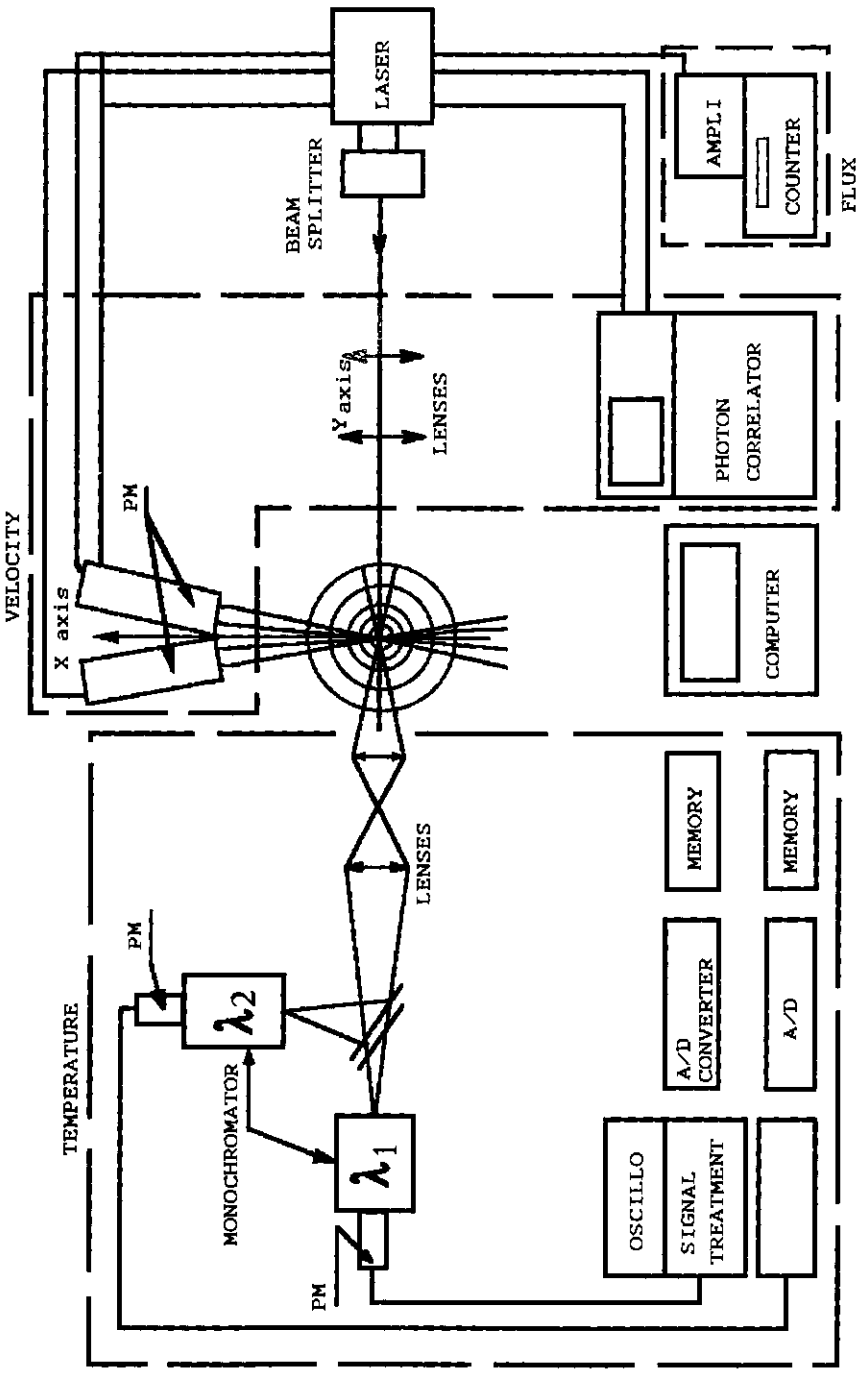

Figure 3-31. System for measuring simultaneously plasma temperature field, plasma velocity field, particle number flux, particle velocity distribution, and particle temperature distribution [34].

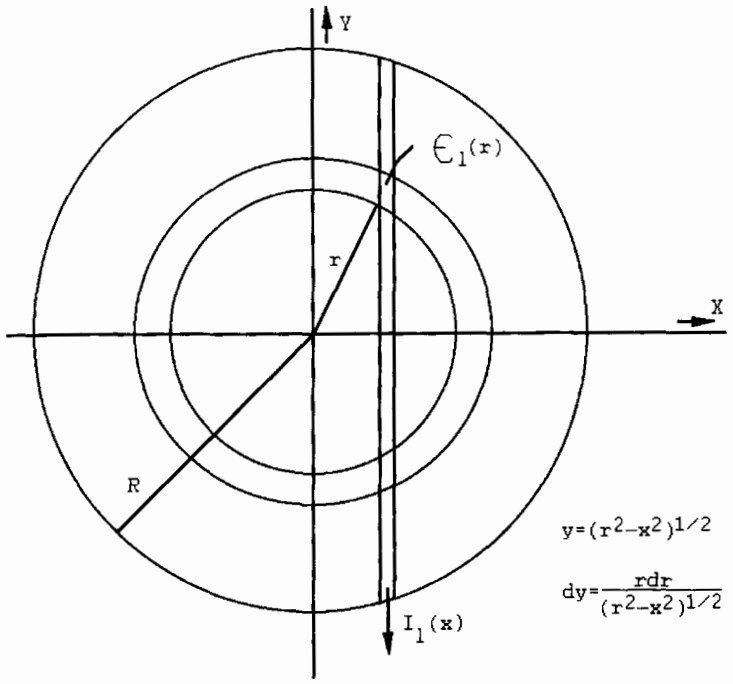

Figure 3-32. Geometric relationship of a plasma volume element used to measure local plasma emissivities ε_l by Abel's inversion [3].

obtained from the observed side-on intensity $I_L(x)$ (Eq. 3-31) by Abel's inversion (Eq. 3-32) according to [3]:

$$I_L(x) = 2\int \varepsilon_L(r)\,dy = 2\int \varepsilon_L(r) r\,dr/(r^2 - x^2)^{1/2} \tag{3-31}$$

$$\varepsilon_L(r) = -(1/\pi)\int [I_L(x)/(x^2 - r^2)^{1/2}]\,dx. \tag{3-32}$$

Figure 3-32 shows the geometric relationships of a plasma volume element of dimensions dx and $dy = r\,dr/(r^2 - x^2)^{1/2}$.

If oxygen is present in the plasma, the temperature can be measured using the rotational states of oxygen molecules and measuring the intensity of the rotation bands (Schumann–Runge bands) in the 336–351 nm range.

Using monochromators equipped with holographic gratings, and x–y stepping-motors to control the displacement of the plasma jet the precision of the measurement is within 5% [35]. Using the temperature determined from the local (relative) emission coefficient, the absolute emission coefficient $\varepsilon_{L,abs}$ can be obtained as

$$\varepsilon_{L,abs} \propto \exp(-E_s/kT)h\nu. \tag{3-33}$$

From the ratio of the absolute emissivities of two spectral lines, $\varepsilon_{L1}/\varepsilon_{L2} \propto \exp[(-E_{s1} - E_{s2})\,kT]$, the relative error of the temperature measurement can be estimated as

$$\Delta T/T = \Delta(E_{s1} - E_{s2})/E_{s1} - E_{s2}. \tag{3-34}$$

With temperature measurements of this type the temperature distribution shown in Fig. 3-25 was measured [28].

3.4.1.2 Two-wavelengths Pyrometry

The temperature of a plasma can also be measured by two-color pyrometry at two wavelengths [34, 36]. While the spectroscopic methods to measure the plasma temperature can be performed in an 'empty' plasma, i.e. without the presence of radiating particles, the two-color (wavelength) pyrometry requires seeding particles such as alumina particles of small diameter (3 μm). Figure 3-31 shows the equipment used by Vardelle *et al.* [34] to measure plasma temperatures. The light scattered by the moving particles was observed off-axis by two photomultipliers directed at angles of 81° and 99° to the optical axis of the laser beam. Measurements were made of the in-flight particle emission at two wavelength, 680 and 837 nm. A monochromator placed in front of each of the photomultipliers was used to define the wavelength of the particle emission by filtering out the background plasma radiation. It is crucial to select wavelengths that are unaffected by neighboring gas emission lines and also to assume that the emissivity of the particles does not change with the wavelength, i.e. that conditions of a grey body radiation prevail. In this case the color temperature of the particles corresponds to their true surface temperature, and the assumption is thus satisfied that the tracer particle temperature reflects faithfully the plasma temperature. By calibration using a tungsten lamp the statistical information provided by the particle emission at the two selected wavelengths can be converted into statistical information about the particle surface, and thus the plasma temperature distribution. It should be emphasized that these assumptions are only satisfied under low-loading conditions, i.e. if local cooling of the plasma due to the presence of particles can be neglected (see Sec. 4.4.1).

Under other simplifying assumption, for example uniform emissivity of the ideally spherical particles over their entire surface area and constant surface temperature along the entire path of observation, the particle temperature can be calculated from

$$T_P = \{C(\lambda_1 - \lambda_2)/\lambda_1\lambda_2\}/[\ln(I_{\lambda 1}/I_{\lambda 2}) + 5\ln(\lambda_1/\lambda_2)], \tag{3-35}$$

where λ_i denote the wavelengths, $I_{\lambda i}$ the measured spectral intensities, and C is a constant. While this technique shows a vast improvement over the spectroscopic methods based on line emissions of gas atoms, there are three principal limitations [34]. The first relates to the presence of background plasma radiation, in particular close to the core of the plasma jet. Therefore no measurements can be made on particles whose trajectories are close to the central axis of the jet. The second limitation results from the rapid decrease of the emission intensity with decreasing surface

temperature. As a consequence the lower temperature limit for successful measurements is around 1 800 K. Finally, the third limitation is due to the long field of depth that requires extremely low particle loading conditions in order to avoid saturating the photoelectric system.

3.4.2 Velocity Measurements

The plasma velocity can be measured with either a Pitot tube probe technique [37, 38] or with a time-of-flight two-point laser anemometer [39, 40]. The first method relies on rather stringent simplifying assumptions made about the local Reynolds numbers, plasma densities and plasma viscosities, the second one is limited by laser beam diffraction, statistical bias towards high velocity particles, inhomogeneous seeding across zones of steep velocity and temperature gradients, and slip between the particle and the plasma velocities which, however, can be reduced by reduced particle size. Despite these limitations both methods are frequently used to estimate plasma jet velocities in order to optimize plasma spray conditions and coating properties.

3.4.2.1 Enthalpy Probe and Pitot Tube Techniques

A water-cooled so-called enthalpy or Grey probe is immersed in a plasma jet to extract a sample of gas. In order to minimize the disturbance of the plasma jet the dimensions of the probe should be as small as possible. Today probes with a diameter as small as 1.5 mm can be used. A tare measurement is required to account for the external heat transfer to the probe [41]. This is accomplished by interrupting the gas stream (no-flow regime) through the Grey probe and measuring the increase of the temperature of the cooling water due to heat transfer from the surrounding plasma. The 'tare' measurement yields

$$\Delta Q_{\mathrm{nf}} = (\mathrm{d}m_{\mathrm{c}}/\mathrm{d}t)c\Delta T_{\mathrm{nf}}, \tag{3-36}$$

with ΔQ_{nf} = difference in heat content at no-flow condition, $\mathrm{d}m_{\mathrm{c}}/\mathrm{d}t$ = mass flow rate of the coolant, c = specific heat, and ΔT_{nf} = temperature rise at no-flow conditions. After opening the sampling valve of the probe, the amount of heat acquired by the probe increases to

$$\Delta Q = (\mathrm{d}m_{\mathrm{g}}/\mathrm{d}t)(h_1 - h_2) + \Delta Q_{\mathrm{nf}} = (\mathrm{d}m_{\mathrm{c}}/\mathrm{d}t)c\Delta T, \tag{3-37}$$

with $\mathrm{d}m_{\mathrm{g}}/\mathrm{d}t$ = mass flow rate of the plasma gas, h_1 = enthalpy of the gas at the inlet temperature, and h_2 = enthalpy of the gas at standard conditions (room temperature). From Eq. 3-37 follows the expression for the stagnation enthalpy:

$$h_1 = h_2 + [\{\mathrm{d}m_{\mathrm{c}}/\mathrm{d}t\, c\}/(\mathrm{d}m_{\mathrm{g}}/\mathrm{d}t)](\Delta T - \Delta T_{\mathrm{nf}}). \tag{3-38}$$

The temperatures are measured with thermocouples, the cooling water mass flow rate with a rotameter or a similar device, and the gas mass flow rate with either a

sonic orifice or a mass flow meter. In the case of a sonic orifice the mass flow rate of the gas is, according to [41]

$$dm_g/dt = C_A\left(p_0/T_0^{1/2}\right)\left[(M/R)\gamma(2/\gamma+1)^{(\gamma+1)/(\gamma-1)}\right]^{1/2}, \tag{3-39}$$

where C_A = effective cross-sectional area of the orifice, p_0 and T_0 = pressure and temperature immediately upstream of the orifice, and γ = adiabatic exponent ($= c_p/c_v$).

The Grey probe cannot be operated continously but can be used during the no-flow regime as a Pitot probe to measure the stagnation pressure, p_{st} and according to Bernoulli's theorem, the free-stream velocity of the plasma jet:

$$v = [2(p_{st} - p_{atm})/\rho]^{1/2}, \tag{3-40}$$

where the plasma gas density ρ must be determined from thermodynamic tables using the plasma temperature determined by the methods described in Sect. 3.4.1. In more detail, for an argon plasma the gas density ρ can be approximated by $\rho = X_{Ar}\rho_{Ar} + X_{Air}\rho_{Air}$. X_{Air} can be determined with a lambda-type oxygen sensor probe based on stabilized zirconia, and ρ_{Ar} and ρ_{Air} from thermodynamic tables. As a check for the validity of the plasma velocity measurement the total mass flow rate of argon can be used according to [3]

$$dm_{Ar}/dt = 2\pi \int (X_{Ar}\rho_{Ar}v)r\, dr \tag{3-41}$$

integrated between the boundaries 0 and r_0 that define the radius of the plasma jet. The energy flux through a given cross-section of such a jet can be expressed by

$$Q = 2\pi \int \rho(r)h(r)v(r)r\, dr, \tag{3-42}$$

where $\rho(r)$, $h(r)$ and $v(r)$ are, respectively the radial density, enthalpy and velocity profiles of the plasma jet within the boundaries 0 to r_0. Figure 3-33 shows the decay of the axial plasma velocity for the currents of 450 and 600 A, and various argon flow rates between 23.6 and 47.2 l min^{-1}. For arc currents around 450 A the change in flow rate has only a small effect on the plasma velocity and its axial decay. An explanation for this may be found by assuming two opposing effects that affect the flow velocity with increasing argon flow rate [41]. Increasing gas flow rates require an increase of the plasma velocity in order to satisfy the continuity equation of mass. This can be achieved only if the plasma temperature remains constant. Higher gas flow rates, however, reduce the temperature thus leading to higher plasma gas densities, and consequently to lower plasma velocities at constant cross-section of the plasma jet. These two opposing phenomena appear to compensate each other at lower arc currents. At higher currents the length of the jet varies considerably with varying gas flow rates, and compensation cannot be achieved anymore. For details on the mea-

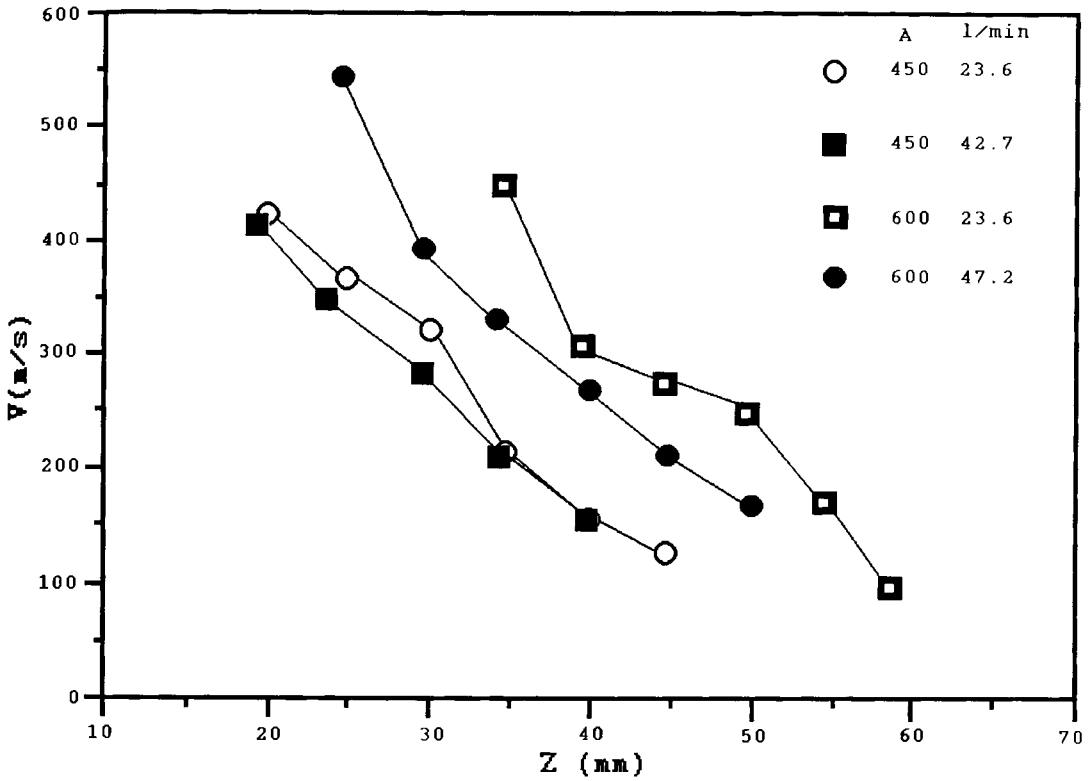

Figure 3-33. Axial velocity decay of an argon plasma measured by an enthalpy probe [41].

surement techniques and typical results the reader is referred to the paper by Capetti and Pfender [41].

3.4.2.2 Laser Doppler Anemometry (LDA)

One of the standard plasma velocity measurement techniques, LDA has emerged as a powerful method of plasma diagnostics. Since it is an optical method it does not interfere with the flow of the plasma. However, the plasma jet must be seeded with very fine powder particles, usually alumina or zirconia [42], carbon or silicon [43] or silicon nitride [44]. Also, a laser pulse of 15 ns duration that produced a plasma drop of high intensity has been used as a tracer [45]. The LDA technique can be used in two modes: *fringe* and *two-point measurement modes*. While the former is mostly used for velocity measurements of larger powder particles in the plasma jet (see Sect. 4.5.1) the latter is being used to measure the supposedly undisturbed plasma velocity via the observation of very small tracer particles [46]. It is essential that the particles must be small enough as not to interfere with the plasma flow but large enough as to not evaporate during their residence time in the hot plasma jet. Also, the method of

seeding is of importance. Adding very fine powder through the powder injection port of a d.c. plasmatron leads to incomplete particle distribution and failure of the particles to penetrate the hot core of the jet. This can be avoided by passing a part of the plasma gas through a fluidized bed consisting of a mixture of very fine and coarse powders [42]. The passing gas extracts selectively the fines and carries them over into the jet.

In the *two-point LDA* measurements [47] the laser beam, after passing through a beam splitter, is focused using a lens of a focal length of 16 mm to form two coherent light beams of 50 μm diameter and 400 μm apart. Those two beams are projected in the plasma jet by a second lens of a focal length of 50 mm (Fig. 3-34). Furthermore each beam is focused onto the entrance slit of two photomultipliers equipped with a narrow-band interference filter (514.5 nm, $\Delta\lambda = 0.25$ nm). By cross-correlating the electrical output of the photomultipliers via a photon correlator, the particle (= plasma) velocity can be determined. When a particle crosses the two beams in the cylindrical measuring volume of 0.6×1.1 mm, it produces two successive light bursts. Their time delay can be used to calculate the velocity.

In the *fringe mode* measurements the two laser beams produced by the beam splitter are focused and allowed to interfere thus forming an interference fringe pattern in the flow region. The interfringe spacing is

$$\delta = \lambda/[2 \sin(\phi/2)], \tag{3-43}$$

where λ = wavelength of the incident laser beam and ϕ = angle of interception of the two laser beams.

When a particle traverses the point of intersection of the two beams a light burst is being produced modulated at a frequency that is a function of its velocity and the fringe spacing δ. The signal output of the photomultiplier is being used to determine the time required for the particle to pass a given number of fringes. After acquisition of a sufficient number of measurements, statistical analysis is carried out giving the minimum velocity, maximum velocity, mean velocity and standard deviation of the particle velocities. From this the probability distribution function is obtained by dividing the velocity window into a number of segments and then counting the number of particles falling into each segment. Eventually the normalized probability distribution function can be calculated from

$$\Pr(v_j) = (m_j/v_j)/\sum (m_j/v_j), \tag{3-44}$$

where m_j = number of particles with a velocity between v_j and v_{j+1}.

Figure 3-35 shows the profiles of the axial plasma velocity (bottom) and the intensity of turbulence in axial and radial directions (top) along the centerline of an Ar/N_2 plasma jet (80 vol% Ar, $dm_g/dt = 23.6\,l\,min^{-1}$, $I = 400$ A, $U = 38$ V, $E = 15.2$ kW) [42]. The centerline plasma velocity is $250\,m\,s^{-1}$ and shows a rapid drop with increasing distance z from the nozzle. Contrary to this, the intensity of turbulence, defined as v'/v, i.e. the ratio of the standard deviation of the velocity to the mean velocity (Fig. 3-35, top) first increases with increasing distance from the nozzle to about 40% at $z = 40$ mm, and then decreases gradually. This is consistent

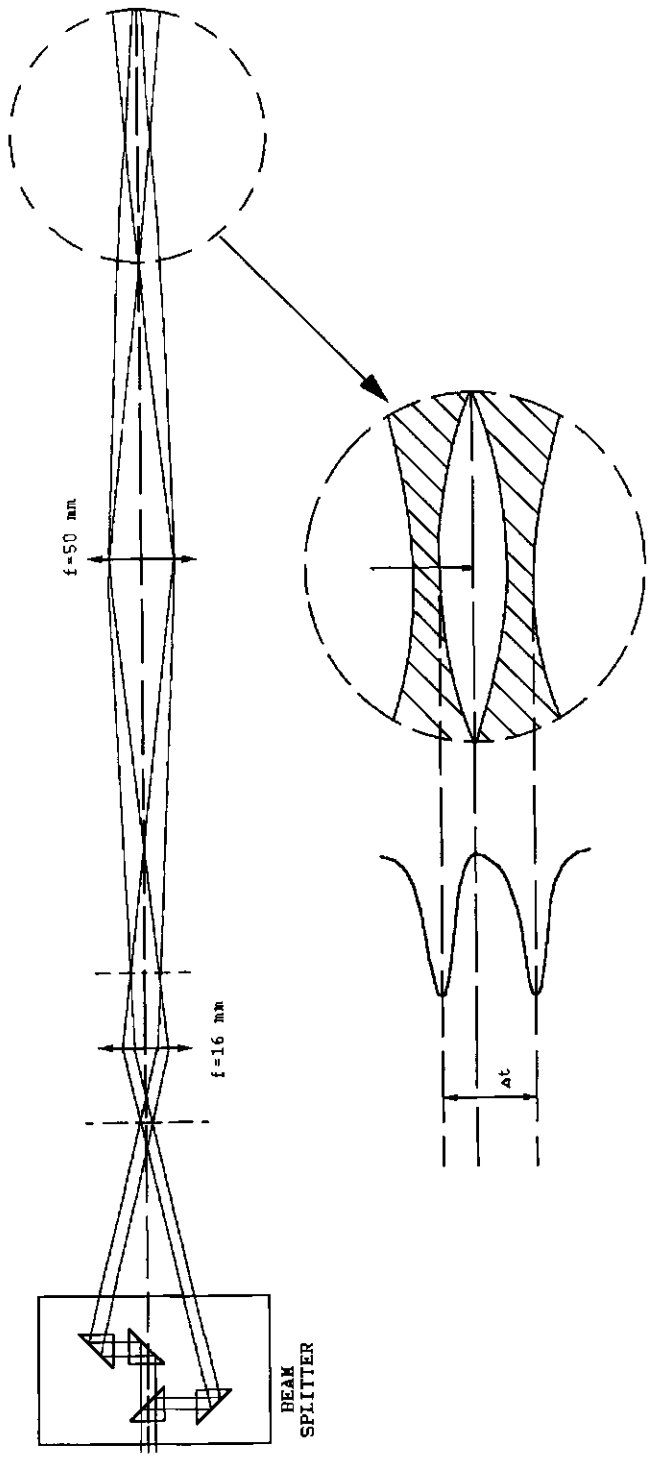

Figure 3-34. Experimental setup of a two-point laser Doppler anemometer (LDA) according to [28].

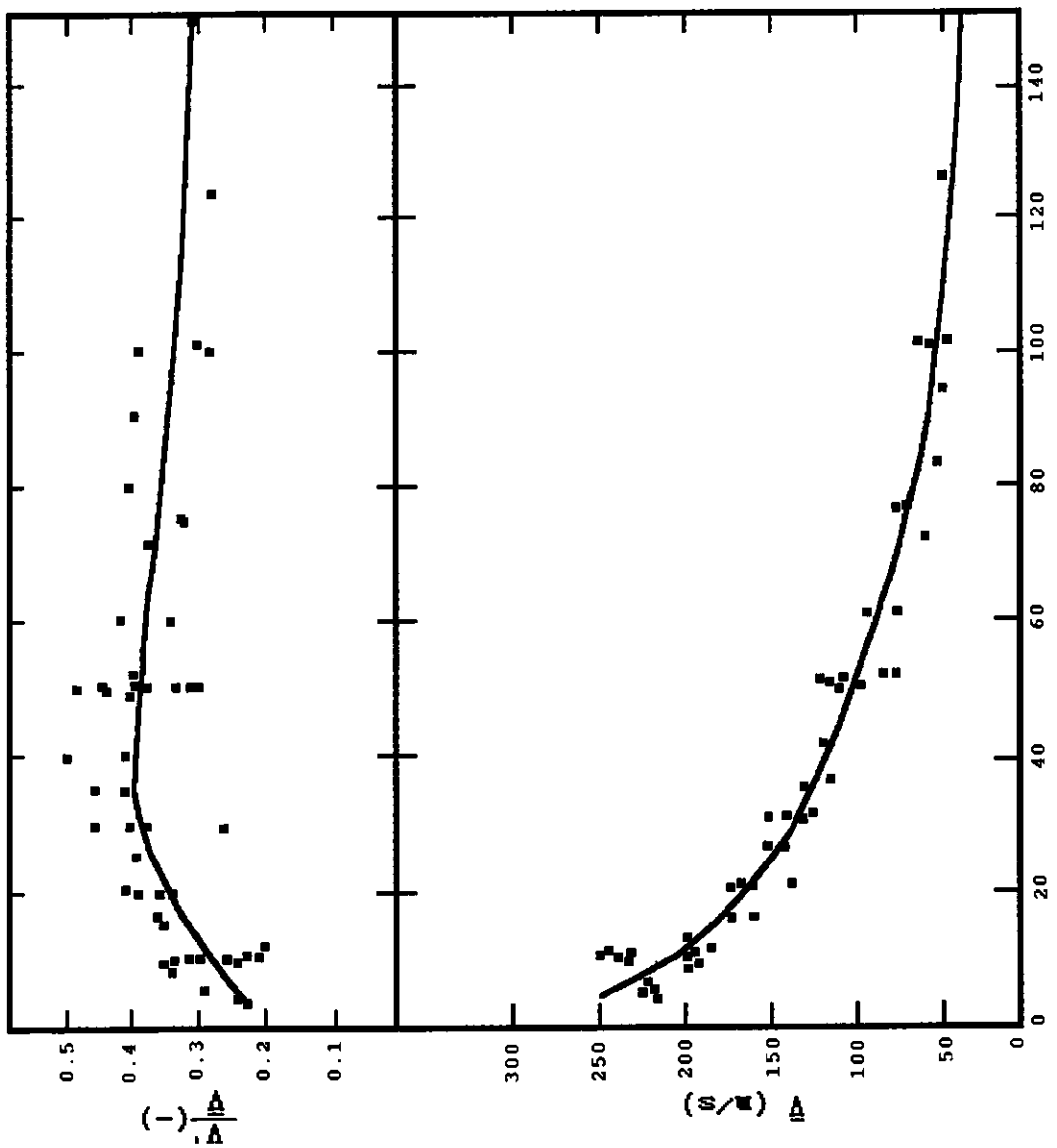

Figure 3-35. Plasma and particle velocities (bottom) and intensity of turbulence (top) along the centerline of an argon/nitrogen (80 vol% argon) plasma jet [42].

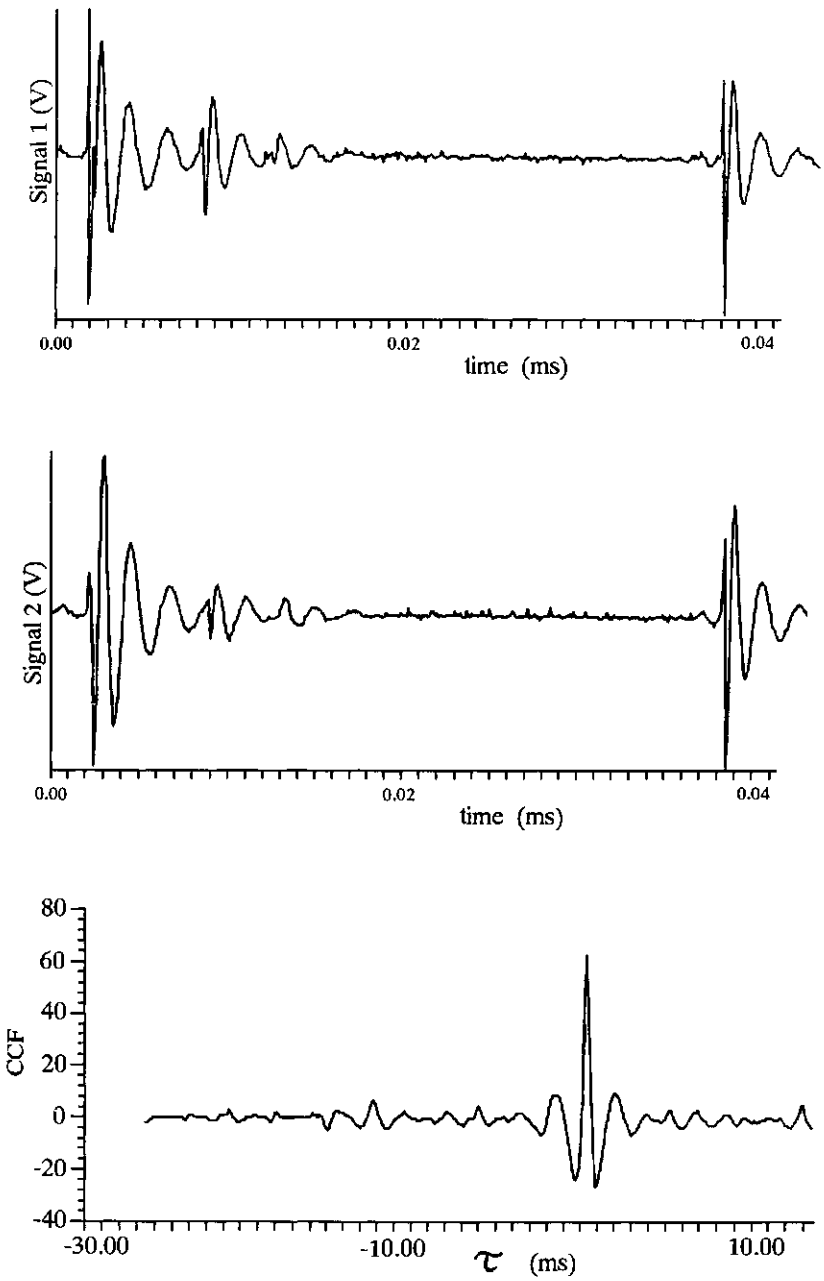

Figure 3-36. Schematic of the cross-correlation method to measure particle velocities [48].

with other findings [28] of the formation of vortices immediately at the exit point of the plasma from the nozzle. This fact has let to approaches to reduce the turbulences in a plasma jet by appropriately formed nozzles such as axially symmetric Laval nozzles that produce parallel and uniform flow, and thus prevent entrainment of cold surrounding gas [33] (see Sect. 3.3.3.2).

3.4.2.3 Other Methods

A different approach to velocity measurements requiring less sophisticated equipment is the *cross-correlation method* [48]. It is based on the measurement of the travel time, t, of powder particles between two observation points in the particle flow direction separated by the distance s. The light emitted from the two observation points will be recorded by two photodiodes. To suppress the plasma light the electrical signals will be filtered through a band pass filter. Figure 3-36 shows two typical signals 1 and 2. Shifting the signals $s_1(t)$ and $s_2(t)$ against each other by a variable time difference τ yields a maximum similarity for $\tau = \tau_{max} = t$. A quantitative expression of this similarity is the cross-correlation function CCF(τ):

$$\mathrm{CCF}(\tau) = \phi_{s(1),s(2)}(\tau) = \int s_1(t) \times s_2(t+\tau)\,\mathrm{d}t. \tag{3-45}$$

The position of the maximum of the CCF (Fig. 3-36, bottom) finally yields the velocity of the streaming plasma, $v = s/t$.

Kuroda *et al.* [49] developed a technique to measure particle velocities *in situ* using a spatial filter without the need of complex optical settings. The technique allows measuring the average particle velocity at dense particle loading. The spatial filter consists of five parallel flat plates at equal intervals, d. A parallel beam passing through the filter is focused into an optical fiber. The filter can be moved horizontally and vertically through a sliding table. When a particle radiating light traverses in front of the filter assembly, four peaks of light intensity are being detected by a photomultiplier placed at the end of the optical fiber. Analysis of the time interval of the peaks, t yields the particle velocity according to $v = d/t$, where d = known interval of the slits. Also, analysis of the power spectrum of the radiated light by an a fast Fourier transform (FFT) analyzer allows calculation of particle velocities by the relationship $f = v/d$, where f = peak frequency.

References

[1] A. Rutscher, *Plasmatechnik. Grundlagen und Anwendungen. Eine Einführung*. Carl Hanser-Verlag, München, Wien, **1982**.

[2] F. Cap, *Einführung in die Plasmaphysik I, Wiss. Taschenbücher*, Bd. 72. Akademie-Verlag Berlin, Pergamon Press Oxford, Vieweg + Sohn Braunschweig, **1970**.

[3] M. I. Boulos, P. Fauchais, E. Pfender, *Fundamentals of Materials Processing using Thermal Plasma Technology*. Canadian University–Industry Council on Advanced Ceramic (CUICAC) Short Course, Edmonton, Alberta, Canada, 17–18 October, **1989**.

[4] P. R. Smy, *Adv. Phys.* **1976**, *25*(5), 517.
[5] I. Langmuir, M. Mott-Smith, *Phys. Rev.* **1926**, *28*, 727.
[6] K. S. Drellishak, Ph.D. Thesis, Northwestern University, Evanstown, IL, **1963** (after [3.3])
[7] H. Edels, IEEE, Vol. 108A, Paper No. 3498, **1961**.
[8] W. Elenbaas, *Physica* **1934**, *1*, 673.
[9] G. Heller, *Physics* **1935**, *6*, 389.
[10] H. Maecker, *Z. Phys.* **1959**, *157*, 1.
[11] J. Mostaghimi, *Trans. 17th Workshop CUICAC* (Ed. R. B. Heimann), Quebec, Canada, 2 October, **1991**.
[12] P. Proulx, J. Mostaghimi, M. I. Boulos, *Proc. ISPC-8*, Tokyo, Japan, **1987**, *1*, 13.
[13] M. Wehrli, *Helv. Phys. Acta* **1928**, *1*, 323.
[14] A. E. Guile, *IEEE Rev.* **1971**, *118*, 1131.
[15] J. D. Cobine, E. E. Burger, *J. Appl. Phys.* **1955**, *27*, 895.
[16] N. Sanders, K. C. Etermadi, E. Pfender, *J. Appl. Phys.* **1982**, *53*(6), 4136.
[17] M. Thorpe, *Chem. Eng. Prog.* **1989**, *July*, 43.
[18] H. Gerdien, A. Lotz, *Wiss. Veröff. Siemens Werke* **1922**, *2*, 489.
[19] T. B. Reed, *J. Appl. Phys.* **1961**, *32*, 821.
[20] H. U. Eckert, *High Temp. Sci.* **1974**, *6*, 99.
[21] M. I. Boulos, M. I. *Pure Appl. Chem.* **1985**, *57*(9), 1321.
[22] J. Mostaghimi, P. Proulx, M. I. Boulos, *J. Plasma Chem. Plasma Proc.* **1984**, *4*, 129.
[23] R. W. Smith, Z. Z. Mutasim, *J. Therm Spray Technol.* **1992**, *1*(1), 57.
[24] T. Yoshida, T. Tani, H. Nishimura, K. Akashi, *J. Appl. Phys.* **1983**, *54*, 640.
[25] T. Takeyama, K. Fukuda, *Development of an all-solid state r.f.-r.f. thermal plasma reactor*, National Chemical Laboratory for Industry, Internal Report, AIST/MITI, Tsukuba, Japan, **1986**, *21*(4).
[26] W. Weizel, R. Rompe, *Theorie elektrischer Lichtbogen und Funken*, Barth, Leipzig, **1949**.
[27] Y. Chang, R. M. Young, E. Pfender, *J. Plasma Chem. Plasma Proc.* **1989**, *9*, 272.
[28] M. Vardelle, A. Vardelle, P. Fauchais, M. I. Boulos, *AIChE J.* **1983**, *29*, 236.
[29] C. V. Boffa, E. Pfender, *Enthalpy probe and spectrometric studies in argon plasma jets*, HTL Tech. Rep. No.73, University of Minnesota, MN, USA, **1968**.
[30] E. Pfender, W. L. T. Chan, R. Spores, *Proc. 3rd NTSC*, Long Beach, CA, USA, 20- 25 May **1990**, 1.
[31] J. Gleick, *Chaos. Making a New Science*. Penguin Books, New York, NY, USA, **1988**.
[32] R. Henne, M. v. Bradke, G. Schiller, W. Schurnberger, W. Weber, *Proc. 12th ITSC*, London, 4–9 June, **1989**, P112, 175.
[33] K. Foelsch, *J. Aeronaut. Sci.* **1949**, *March*, 161.
[34] M. Vardelle, A. Vardelle, P. Fauchais, M. Boulos, *AIChE J.* **1988**, *34*, 567.
[35] A. Vardelle, M. Vardelle, P. Fauchais, *J. Plasma Chem. Plasma Proc.* **1982**, *3*, 255.
[36] J. Mishin, M. Vardelle, J. Lesinski, P. Fauchais, *J. Phys. E.: Sci. Instrum.* **1987**, *20*, 620.
[37] J. Grey, P. F. Jacob, M. P. Sherman, *Rev. Sci. Instrum.* **1962**, *33*(7), 738.
[38] J. B. Cox, F. J. Weinberg, *J. Phys. D.: Appl. Phys.* **1971**, *4*, 877.
[39] G. Gouesbet, *Plasma Chem. Plasma Proc.* **1985**, *5*, 91.
[40] L. E. Drain, *The Laser Doppler Technique*, Wiley, New York, **1980**.
[41] A. Capetti, E. Pfender, *Plasma Chem. Plasma Proc.* **1989**, *9*, 329.
[42] J. Lesinski, M. I. Boulos, *Plasma Chem. Plasma Proc.* **1988**, *8*, 113.
[43] J. Lesinski, M. I. Boulos, *Plasma Chem. Plasma Proc.* **1988**, *8*, 133.
[44] T. Yoshida, T. Tani, H. Nishimura, K. Akashi, *J. Appl. Phys.* **1983**, *54*, 640.
[45] C. J. Chen, *J. Appl. Phys.* **1966**, *37*, 3092.
[46] B. Richards (ed.), *Measurements of Unsteady Fluid Dynamic Phenomena*, McGraw Hill, New York, **1977**.
[47] M. Vardelle, A. Vardelle, P. Fauchais, M. I. Boulos, *AIChE J.* **1982**, *29*, 236.
[48] M. Kloke, *Proc. 3rd Workshop 'Plasma Technology'*, Ilmenau, Germany, 22–23 June, **1995**.
[49] S. Kuroda, T. Fukushima, S. Kitahara, H. Fujimori, Y. Tomita, T. Horiuchi, *Proc. 12th ITSC*, London, 4–9 June, **1989**, P27-1.